

# THE UNIQUE STRUCTURAL PARAMETERS OF THE UNDERLYING HOST GALAXIES IN BLUE COMPACT DWARFS

STEVEN JANOWIECKI<sup>1</sup> AND JOHN J. SALZER<sup>1</sup>  
(Received 8 Apr 2014; Accepted 6 Aug 2014)  
*Draft version April 22, 2022*

## ABSTRACT

The nature of possible evolutionary pathways between various types of dwarf galaxies are still not fully understood. Blue compact dwarf galaxies (BCDs) provide a unique window into dwarf galaxy formation and evolution and are often thought of as an evolutionary stage between different classes of dwarf galaxies. In this study we use deep optical and near-infrared observations of the underlying hosts of BCDs in order to study the structural differences between different types of dwarf galaxies. When compared with dwarf irregular galaxies of similar luminosities, we find that the *underlying hosts* of BCDs have significantly more concentrated light distributions, with smaller scale lengths and brighter central surface brightnesses. We demonstrate here that the underlying hosts of BCDs are distinct from the broad continuum of typical dwarf irregular galaxies, and that it is unlikely that most dwarf irregular galaxies can transform into a BCD, or vice versa. Furthermore, we find that the starburst in a BCD only brightens it on average by  $\sim 0.8$  mag (factor of 2), in agreement with other studies. It appears that BCDs are a long-lived and distinct type of dwarf galaxy which exhibit an exceptionally concentrated matter distribution. We suggest that it is this compact mass distribution that enables the strong star-formation events that characterize this class of dwarf galaxy, that the compactness of the underlying host can be used as a distinguishing parameter between BCDs and other dwarf galaxies, and that it can also be used to identify BCDs which are not currently experiencing an intense starburst event.

*Subject headings:* galaxies: dwarf, galaxies: evolution, galaxies: structure

## 1. INTRODUCTION

With the exception of mergers and interactions between galaxies, star formation is the most transformative process that a galaxy can undergo. Star formation in large gas-rich spiral galaxies is a very complex process that depends on many internal and environmental factors. Alternatively, gas-rich dwarf irregular galaxies (dIIs) provide a much simpler laboratory for studying star formation processes in galaxies. In particular, Blue Compact Dwarf galaxies (BCDs) are especially unique objects, as they are currently experiencing some of the most intense bursts of star formation in the local universe.

The term “Blue Compact Dwarf” is used in the literature to describe a wide variety of galaxies. BCDs were first identified by Sargent & Searle (1970) as small galaxies with emission lines in their spectra, giving the appearance of “extragalactic HII regions”. It is clear that BCDs are relatively rare galaxies undergoing a significant starburst and that they have characteristically low metallicities. However, conclusions about the origin and nature of BCDs depend strongly on sample selection. Indeed, there are many different definitions of BCDs in the literature (e.g., Thuan & Martin 1981, Gil de Paz et al. 2003).

Soon after their discovery, the very blue colors of BCDs were found to be consistent with bursting late type dwarfs (Searle, Sargent, & Bagnuolo 1973). The combination of these blue colors with their very low metallic-

ities led some to propose that BCDs were young galaxies possibly undergoing their first episode of star formation (Searle & Sargent 1972). Indeed, even modern observations (e.g., I Zw 18, Izotov & Thuan 2004) have concluded that some BCDs are intrinsically young (i.e.,  $< 500$  Myr old) objects. However, whenever more sensitive observations are made (e.g., Aloisi et al. 2007), evolved stars are detected and it is clear that all of the known BCDs have an underlying old stellar population. Indeed, the discovery of an underlying lower surface brightness component (Loose & Thuan 1986) in BCDs was another confirmation that old stars are an important component in BCDs, meaning that they are not young objects or purely HII regions. While suggestions have been made that there may be a small fraction of intrinsically young galaxies (Thuan et al. 1999), the most recent searches have revealed older, underlying stellar hosts in all BCDs (Papaderos et al. 2008).

Since its discovery, the lower surface brightness component in BCDs has been studied in the search for evolutionary connections between dwarf galaxies. Lin & Faber (1983) suggested that dwarf spheroidal galaxies (dSph) could form when a dI loses its gas from ram pressure stripping near a large galaxy. However, Thuan (1985) found that the infrared colors of dwarf elliptical galaxies (dEs) and dIs imply metallicities that are quite different; simple gas stripping is not enough to transform a dI into a dE. Adding to these differences, Papaderos et al. 1996 found that the underlying host structure of BCDs was substantially different from dIs and dEs, which means that the older stellar component must undergo serious structural changes if there are evolutionary connections between types of dwarf galaxies. This structural distinc-

sjanowie@astro.indiana.edu, slaz@astro.indiana.edu  
<sup>1</sup> Department of Astronomy, Indiana University, 727 E 3rd St, Bloomington, IN 47405

tion in the underlying stellar component of dIs and BCDs has also been noted by Marlowe et al. (1999), Salzer & Norton (1999), and Doublier et al. (1999).

More recently, these types of structural decompositions have been carried out on more types of galaxies, in order to find evolutionary similarities at other mass ranges. In particular, Luminous Blue Compact Galaxies (LBCGs, Werk et al. 2004, Garland et al. 2004, Salzer et al. 2009) have been fitted with a variety of profile shapes (Micheve et al. 2013, Amorín et al. 2009), as have the so-called Green Pea Galaxies (Cardamone et al. 2009). In general, the LBCGs and BCDs are both dominated in their appearance by recent and intense star formation, and the LBCGs may be higher-mass analogues to BCDs. If the transformative effects of star formation can have a substantial impact in the more massive LBCGs, the effects of recent star formation in BCDs will be even more significant.

To understand the evolutionary status of galaxies currently hosting BCD-like starbursts, we have acquired observations of a sample of BCDs with high resolution and in many wavelengths. In this paper we compare the isophotal structures of BCDs with other types of dwarf galaxies to shed light on possible evolutionary connections. In a subsequent paper we fit the Spectral Energy Distributions (SEDs) of these BCDs with models to derive star formation histories and further constrain evolutionary pathways.

Many of the BCDs in our sample have been observed with space- and ground-based telescopes. Indeed, the literature is rich with high quality surface brightness profiles, some with even better resolution and depth than the observations presented here. However, most studies of the structural parameters of BCDs are carried out in great detail but on only a handful of objects. The structural parameters obtained from fitting surface brightness profiles can be affected by the methods used or even the observations themselves. In order to avoid systematic uncertainties inherent in a heterogeneous sample, we will use only our own observations to determine structural parameters for our sample of BCDs.

This paper is organized as follows: In Section 2 we present our BCD sample and the observations we have obtained. Our surface photometry methods and fits are described in Section 3 and the results of those fits are compared with other dwarf galaxies in Section 4. Finally, we discuss the implications of these results and summarize our conclusions in Section 5.

## 2. SAMPLE AND OBSERVATIONS

Our sample of 21 BCDs represents a variety of BCDs and BCD-like galaxies, some of which are archetypal BCDs (e.g., I Zw 18) and some of which may be similar to dEs but possess a strong central starburst (e.g., Mk 900). The sample includes a wide range of BCD morphologies, including BCDs with offset starbursts (e.g., Mk 36, Mk 750), BCDs with two primary starburst regions (UM 461, Mk 600), BCDs with cometary shapes in their outer isophotes (e.g., Mk 5), and BCDs with a large number of active star formation sites (e.g., UM 439, UM 462, UM 323).

Our BCDs are all less luminous than  $M_B = -18$  (typically around  $M_B \sim -16$ ), have blue colors with  $B-V \sim 0-0.5$ , and are less than 50 Mpc distant (their

median distance is 16 Mpc). Gas phase abundances ( $Z = 12 + \log(O/H)$ ) show that our sample is characteristically metal poor, with a range between  $Z = 7.18$  (I Zw 18) and  $Z = 8.64$  (Mk 328), although the vast majority have metallicity between 7.7 and 8.2; the median value is  $Z = 7.96$ .

Table 1 gives the details of our BCD sample. Coordinates on the sky, observed recession velocities, and flow-model distances all come from NED<sup>2</sup> (NASA Extragalactic Database). Our absolute magnitudes come from aperture photometry of the galaxies, using photometric zeropoints from stars in the field measured by SDSS and 2MASS (see Section 2.2 and Section 2.3), and are corrected for Galactic extinction. Also shown are the total integration times from our broadband optical, near-infrared, and narrow band observations. We varied the integration times on each target depending on their expected brightness and sky conditions. Mk 750 was not observed in near-infrared.

### 2.1. Observations

In order to measure the structural parameters of the underlying host galaxies of our BCDs, we need very deep images that are sensitive to their faint outer reaches. Many of the BCDs in our sample have been studied before, but previous surface photometry lacked the necessary depth and sensitivity to measure the structure of the host galaxies. We find that our understanding of the evolutionary context of BCDs requires detailed knowledge about the structure of their faint underlying host galaxies.

If BCDs are typical dwarf galaxies undergoing a recent and localized burst of star formation, their underlying old stellar population should be similar to normal dwarf galaxies. It is easier to separate this old population from the recently-formed stars by considering only the underlying host galaxies of the BCDs. We restrict our surface brightness profile fits to this underlying host light in the outskirts of the BCDs. While the high surface brightness regions of the BCDs typically have clumpy and irregular morphologies, the outskirts have more regular shapes and smoother light distributions. It is this underlying host galaxy that we fit in order to probe the BCD as it was before the current burst of star formation.

Given the very blue optical colors of our BCDs, we chose to observe them in the Johnson B filter in order to achieve the greatest sensitivity to the faint stellar populations of the underlying host galaxy. While this is the optimal filter choice for a metal-poor population, some of the blue light in the BCDs also comes from their substantial ongoing star formation. This recent star formation can be identified by bright  $H\alpha$  emission from the ionized gas around young massive stars. We observe each BCD in a narrow-band  $H\alpha$  filter to locate regions with active star formation. We use these  $H\alpha$  images to mask out regions of the B image involved in current star formation and keep only light from the underlying host galaxy.

A more direct way to study the underlying host galaxy light is to use a much redder filter which is mainly sen-

<sup>2</sup> This research has made use of the NASA/IPAC Extragalactic Database (NED) which is operated by the Jet Propulsion Laboratory, California Institute of Technology, under contract with the National Aeronautics and Space Administration.

TABLE 1  
THE BCD SAMPLE

Name (1)	$\alpha$ (J2000) (2)	$\delta$ (J2000) (3)	$v$ [km/s] (4)	$D$ [Mpc] (5)	$M_B$ [Mag] (6)	$M_H$ [Mag] (7)	$Z$ (8)	$t_B$ [s] (9)	$t_{H\alpha}$ [s] (10)	$t_H$ [s] (11)
UM 323	01 26 46.6	-00 38 46	1913	25.6	-16.10	-17.90	7.96 <sup>1</sup>	1800	1440	3600
UM 408	02 11 23.4	+02 20 30	3598	47.5	-16.04	-17.72	7.74 <sup>1</sup>	1800	1440	4680
Mk 600	02 51 04.6	+04 27 14	1008	13.6	-15.55	-17.30	7.94 <sup>1</sup>	1800	1440	3600
Mk 5	06 42 15.5	+75 37 33	792	15.3	-15.18	-17.74	8.06 <sup>1</sup>	3600	1440	2160
CG 10	09 12 51.7	+31 40 51	1902	30.7	-15.01	-17.47	-	1800	2160	2160
I Zw 18	09 34 02.0	+55 14 28	751	14.6	-14.68	-15.19	7.18 <sup>1</sup>	1800	1440	3600
Was 5	10 10 32.8	+22 00 39	1259	23.1	-15.05	-16.86	7.85 <sup>3</sup>	1800	1440	2160
Mk 36	11 04 58.5	+29 08 22	646	8.4	-14.23	-16.03	7.82 <sup>1</sup>	1800	1440	2880
UM 439	11 36 36.8	+00 48 58	1099	15.9	-16.11	-18.23	8.08 <sup>1</sup>	1800	2160	2160
Mk 750	11 50 02.6	+15 01 23	749	5.2	-13.42	-	8.18 <sup>3</sup>	1800	2160	-
UM 461	11 51 33.3	-02 22 22	1039	12.7	-14.40	-15.87	7.81 <sup>4</sup>	1800	1440	2160
UM 462	11 52 37.3	-02 28 10	1057	13.5	-16.18	-18.07	7.80 <sup>4</sup>	1800	1440	2160
Mk 67	13 41 56.5	+30 31 10	932	18.7	-15.16	-17.42	8.08 <sup>1</sup>	1800	1440	2880
Mk 475	14 39 05.4	+36 48 22	583	11.9	-14.28	-16.25	7.93 <sup>1</sup>	1800	1440	2160
Mk 900	21 29 59.6	+02 24 51	1152	18.9	-17.16	-19.85	8.07 <sup>1</sup>	1800	2160	2160
Mk 324	23 26 32.8	+18 15 59	1600	23.2	-16.70	-19.08	8.18 <sup>2</sup>	1800	1440	2160
Mk 328	23 37 39.5	+30 07 46	1379	20.6	-16.57	-19.57	8.64 <sup>2</sup>	1800	1440	4320

NOTE. — Column 5: distances come from flow models; Column 6: B absolute magnitude; Column 7: H absolute magnitude; Column 8: gas phase abundance  $Z = 12 + \log(O/H)$ ; <sup>1</sup>:  $T_e$  abundances from Zhao et al. 2010; <sup>2</sup>:  $N_2$  abundance from Zhao et al. 2010; <sup>3</sup>: Brinchmann et al. 2008; <sup>4</sup>: Izotov et al. 2007. Columns 9,10,11: exposure times for each filter

sitive to the light from evolved stars and which is much less affected by recently formed stars. Toward this end, we use the near-infrared (NIR) H filter at  $\lambda \sim 1.7\mu m$  to directly observe the old stellar populations of the host galaxies. Very young ( $\sim 5$  Myr) stellar populations can have B-H  $\sim 0$ , but old ( $\sim 10$  Gyr) stellar populations have B-H  $\sim 4$  (Bressan et al. 2012, Girardi et al. 2010, c.f. Carter et al. 2009). Although the BCDs are much fainter and harder to observe in H than in B, the NIR light is more representative of the old underlying component.

We observed our sample of BCDs using the Wisconsin Yale Indiana NOAO (WIYN<sup>4</sup>) 3.5m telescope at Kitt Peak National Observatory<sup>6</sup>, between November 2008 and April 2010. The Minimosaic and OPTIC (Orthogonal Parallel Transfer Imaging Camera) imagers were used to obtain deep images in broadband B and narrow-band H $\alpha$  filters, and WHIRC (WIYN High Resolution Infrared Camera, Meixner et al. 2010) was used to obtain deep near-infrared images in the H filter. The good native seeing of the WIYN site provides images with an average of 1'' seeing. The following subsections describe the individual observations and processing.

## 2.2. Deep B Imaging with WIYN

The B images of the BCDs were observed with the Minimosaic and OPTIC imagers. Minimosaic and OPTIC both consist of two side-by-side 2048 x 4096 pixel CCDs, where the pixels are 0.141'' on a side, and the field-of-view is 10'. Targets were placed on the cosmetically cleanest area of both cameras while avoiding the

<sup>5</sup> The WIYN Observatory is a joint facility of the University of Wisconsin-Madison, Indiana University, Yale University, and the National Optical Astronomy Observatory.

<sup>6</sup> Kitt Peak National Observatory, National Optical Astronomy Observatory, which is operated by the Association of Universities for Research in Astronomy (AURA) under cooperative agreement with the National Science Foundation.

small chip gaps. Two 900s (or three 600s) exposures were taken in B to aid in cosmic ray rejection. One galaxy (Mk 5) was observed twice as long to compensate for poor sky transparency during the observations.

These images were reduced with the standard IRAF<sup>8</sup> CCDPROC and MSCRED packages, including an overscan subtraction, bias image correction, and sensitivity correction from dome flat fields. Laplacian cosmic ray rejection was applied to individual images with LACOS (van Dokkum 2001), a world coordinate system (WCS) was applied using the USNO-B1 catalog, and MSCIMAGE was used to create single-extension images from the multi-extension images. Finally, the individual images of each BCD were combined to create a single, deep image by averaging and using standard bad pixel masks.

Many of the B observations were not taken under photometric conditions, so we use a boot-strap calibration from the Sloan Digital Sky Survey (SDSS) Data Release 9 (Ahn et al. 2012). All but one of the BCDs (Mk 5) are within the survey footprint. Using broadband observations from another observing run with Minimosaic during photometric conditions where standard stars were observed (Haurberg et al. in preparation), we derived our own empirical conversions between SDSS ugriz photometry and Minimosaic BVR photometry, and found the following relationship for B as a function of g and r:

$$B = g + (0.266 \pm 0.036)(g - r) + (0.258 \pm 0.021).$$

We measure the brightnesses of foreground stars on the same chip and amplifier as the BCDs in our B images and find a zero-point for each image based on the difference between the SDSS catalog photometry and our measured

<sup>8</sup> IRAF is distributed by the National Optical Astronomy Observatory, which is operated by the Association of Universities for Research in Astronomy (AURA) under cooperative agreement with the National Science Foundation.

photometry. We selected unsaturated stars with  $r < 22$  mag, and with photometric measurements better than  $\sim < 0.05$  mag. Typical uncertainties (standard deviations of multiple stars in each image) on these computed zero-points are  $0.03 - 0.04$  mag. We use these boot-strap calibrations for all  $B$  photometry throughout this work for consistency. The final calibrated  $B$  images are shown in the left-most column of Figure 1.

We also find a small systematic offset between this aperture photometry and earlier  $B$  photometry (Salzer, private communication), such that the new observations are  $\sim 0.16$  magnitudes brighter, with a standard deviation of only  $\sim 0.10$  magnitudes. This systematic difference could be related to the increased depth of our new observations which may have detected previously unseen low surface brightness light in the outskirts of the BCDs.

### 2.3. Deep $H\alpha$ Imaging with WIYN

The narrow-band  $H\alpha$  images of the BCDs were obtained with Minimosaic, placing the targets on the cosmetically optimal portion of the detector, as with the  $B$  images. We used two narrow-band  $H\alpha$  filters appropriate to the redshift of the targets (90% widths:  $6554 - 6600\text{\AA}$  and  $6596 - 6646\text{\AA}$ ). As with the  $B$  images, in order to effectively reject cosmic rays, two 720s narrow-band exposures were taken of each target. A short (180s) image in the  $R$  filter (encompassing the narrow-band filters in wavelength range) was taken between the pairs of narrow-band exposures to provide an image for subtraction of the stellar continuum. The same image reduction methods were applied as with the  $B$  images.

We remove the continuum from our  $H\alpha$  images by re-scaling the short  $R$  filter exposure, following a well-documented procedure (Van Sistine et al. in preparation). We first align the three images to match each other and apply a WCS using 2MASS stars in the field. Next we measure the full width at half-maximum (FWHM) of the profile of many stars in the three images to identify any mismatches in image quality through the sequence. In order to have effective continuum-subtraction, the images must be at approximately the same resolution. If the average FWHM differs between images by more than  $0.2''$ , the image with the smaller FWHM is smoothed with a Gaussian kernel to match the larger FWHM. Finally, stellar photometry is carried out in all three images, and the images are multiplicatively scaled so that stars, which we assume have no significant  $H\alpha$  emission on average, have the same flux in all images. To produce the final continuum-subtracted image, the scaled  $R$  image is subtracted from the average of the two  $H\alpha$  images.

Due to non-photometric conditions, standard stars were not observed during our  $H\alpha$  observations. However, we again use the calibrated photometric narrow-band Minimosaic observations from Haurberg et al. (in prep) to calculate a typical offset between photometry of stars in the  $R$  and  $H\alpha$  images. We find that the two filters have a consistent zero-point offset of  $3.39 \pm 0.03$  magnitudes. Finally, we compare the photometry of well-measured stars from the images to derive a relationship between calibrated SDSS magnitudes and Minimosaic  $R$  and find the following relationship:

$$R = r + (-0.142 \pm 0.038)(g - r) + (-0.108 \pm 0.023).$$

We adopt the assumption that the narrow-band images here have no significant color term. Thus, we use this relation to derive zero-points for our  $R$  images, and the standard offset between  $R$  and  $H\alpha$  zeropoints to calibrate our  $H\alpha$  images. These  $H\alpha$  images are reprojected using IRAF’s MSCIMAGE task to be matched precisely on the same pixel scale as the  $B$  images. The final calibrated  $H\alpha$  images are shown in the right-most column of Figure 1.

### 2.4. Deep $H$ Imaging

The  $H$  images of the BCDs were observed between Nov 2008 and Sep 2009 with the WHIRC imager. WHIRC has a  $2048 \times 2048$  HgCdTe array with  $0.1''$  pixels and a  $3.3' \times 3.3'$  field-of-view. Total exposure times were between 2200s and 4600s per object.

The most important step in reducing ground-based NIR observations is the sky subtraction. Atmospheric OH emission contributes heavily to the bright ( $\sim 14$  mag/arcsec<sup>2</sup>) near-infrared sky. With this high sky background in mind, we used dithered sequences of 3-minute exposures on each target. Since the BCDs are much smaller than WHIRC’s field-of-view, most of the image is sky and a good sky subtraction can be obtained without separate dedicated sky observations. We dithered in a  $2 \times 2$  box  $50''$  on a side, and offset subsequent dither boxes by  $10''$ . Most targets had 12 three-minute exposures (3 separate  $2 \times 2$  dithers), but we spent more time (up to 26 three-minute exposures) on the fainter targets.

These images were reduced with standard IRAF routines, but required some special attention and efforts, described in detail in Appendix A. In brief, the WHIRC task WPREP is run to trim and linearize all of the raw images. Dome flat fields were created by subtracting an average of 10 lamps-off flat fields from an average of 10 lamps-on flat fields, to remove the very high background (Alam & Predina 1999). These dome flats were also used to create a bad pixel mask. Later on in the reduction process we created sky flat fields that flattened the observations significantly better than the dome flats. Finally, we took darks at every exposure time we planned to use, since the dark level on WHIRC is not negligible.

To achieve a successful sky subtraction we used an iterative subtraction method with object masking. On each iteration, we use the combined images to mask out objects from the individual dithered frames, generate an improved sky subtraction, and then create better combined images. We also found it necessary to characterize and remove a dark “palm-print” feature from some images, which resulted from an issue with the amplifier electronics. The complete details of the sky subtraction and image processing are detailed in Appendix A.

After the final images are created we measured the brightnesses of all of the 2MASS stars in our frames to determine a photometric zero-point for each image. The final calibrated images are re-projected using MSCIMAGE to match the pixels in the  $B$  images ( $0.14''$ ) for consistent surface photometry. The final calibrated  $H$  images are shown in the left-center column of Figure 1, using  $2 \times 2$  pixel binning ( $0.28''$  pixels) to increase the signal-to-noise ratio in each pixel.

### 2.5. SDSS image processing

We also download calibrated *ugriz* images from SDSS DR9 (Ahn et al. 2012) for the BCDs in our sample (excluding Mk 5, which has not been observed by SDSS). These images have average FWHM of  $1.3''$  but are not as deep as our observations. Using IRAF’s MSCIMAGE task and the compatible WCS on the SDSS images and our own, we re-project each SDSS filter image to match the pixels in our *B* image. While less deep than our observations, we use these *ugriz* images to construct surface brightness profiles in additional colors across the high surface brightness regions of the BCDs. This variety of colors is useful to compare with our deep *B – H* color profiles. In particular, we convert the *g – r* surface color profile into a *B – V* profile.

### 2.6. WISE catalog photometry

In order to more directly probe the intrinsic stellar mass of the BCDs, we use infrared observations from the Wide-field Infrared Survey Explorer (WISE, Wright et al. 2010) catalog. WISE surveyed the sky in 4 photometric bands between  $3.4\mu\text{m}$  (*w1* band) and  $22\mu\text{m}$  (*w4* band). The recent AllWISE Data Release (<http://wise2.ipac.caltech.edu/docs/release/allwise/>) contains the most reliable photometric catalog of sources released to date. In particular, we have obtained catalog aperture photometry for all of our BCDs by finding the nearest WISE source within  $5''$  of our BCDs. These infrared luminosities are easily converted into stellar masses via the reliable mass-to-light ratio of McGaugh & Schombert (2013), and will be even less affected by the recent star formation than the near-infrared observations.

### 2.7. Multi-wavelength images

Our observations in *B*, *H*, and  $H\alpha$  for each BCD are shown in Figure 1. Most images are shown using a logarithmic intensity scaling to adequately show the high dynamic range between both the high and low surface brightness portions of each galaxy. The *B* and *H* images are shown in units of calibrated surface brightness (magnitudes per square arcsecond,  $\text{mag}/\text{arcsec}^2$ ) and visibly demonstrate the range of morphologies of BCDs in our sample. For most of our sample, we also produce *B – H* color maps, which are shown in the third column of Figure 1. For Mk 750 we do not have an *H* image and thus cannot create a *B – H* color map. We also do not show a *B – H* color map for UM 461 because our *H* image of UM 461 is not sensitive enough.

While the *B* and *H* images look generally similar to each other, the *B – H* color maps show that there are significant color differences within the BCDs. In particular, many BCDs (c.f. UM 439) have regions of significantly bluer (*B – H*) color which also correspond to regions of stronger  $H\alpha$  emission, likely indicating the locations of HII regions with hot young stars ionizing the low-metallicity gas that surrounds them. Across most of the sample there is a (*B – H*) color trend for the galaxies to have somewhat bluer centers and somewhat redder outskirts, which likely indicates the different stellar populations present across the galaxies.

While many of our BCDs have already been observed by other researchers and have published surface bright-

ness profiles, we restrict our analysis to those profiles which we have observed and processed with our simple and consistent method. One of the largest sample of modern high quality observations is Mischeva et al. 2013, which includes multi-wavelength (*UBVRHK*) surface photometry of 24 Blue Compact Galaxies, three of which are common to our study (UM 439, UM 461, & UM 462). Gil de Paz & Madore (2005) present *BRH* surface photometry of 114 BCDs, with many in common to our study. Hunter & Elmegreen (2006) study the profiles of  $\sim 100$  dIs and BCDs with deep *UBV* and some *JHK* photometry. Finally, Mk 36, UM 408, and UM 461 have been observed in *JHK* with higher resolution and greater depth (Lagos et al. 2011) than in our work.

## 3. SURFACE PHOTOMETRY AND FITTING

Our objective is to measure the properties and structure of the *B* and *H* light of the underlying host in each of our BCDs. While some regions of each BCD are dominated by the light from the recent starburst, the outskirts are dominated by the light from old stars. We use our calibrated  $H\alpha$  images to identify and mask areas of active star formation in our *B* images. The *B*-filter light comes mostly from stellar emission, particularly from young, recently-formed stars. In order to compare BCD profiles with other types of dwarf galaxies, independent of recent star formation we use the  $H\alpha$  threshold masks to ensure that we only fit the light from the old stars and that our surface brightness profile fit represents the light from the underlying host galaxy.

We use the GALPHOT package and ELLIPSE (Jedrzejewski 1987) task in IRAF to fit elliptical isophotes to the *B* images. Starting from an initial isophote, the fit proceeds toward the center of the galaxy until it runs out of pixels to fit, and then proceeds toward the outskirts of the galaxy. At each isophote, the algorithm varies the geometric parameters (center, ellipticity, position angle) of subsequent ellipses until it best fits the galaxy at that isophotal level. Below a certain signal-to-noise threshold, there is not enough galaxy light to accurately determine the shape of the isophotes, so the parameters from the last well-determined ellipse are held fixed and all larger ellipses have the same ellipticity and position angle.

The *B* images are fit both with and without the  $H\alpha$  masks, and we find that the mask has a negligible effect outside of the bright, central region of the galaxy. As our profile fitting will be limited to the outskirts of the galaxies, these  $H\alpha$  masks will not drive our results but are a good precaution. However, to display sensible *B* surface brightness profiles inside the regions excluded by the  $H\alpha$  masks, we need to make a composite profile. When fitting inwardly on the unmasked image, we hold the shape parameters fixed within the region covered by the mask. In detail, we determine the innermost isophote with at least half of its pixels unmasked, and use that as the transition point between an unconstrained shape fit, and holding the shape fixed all the way to the center.

The resulting isophotal ellipse fits obtained from the *B*-filter surface photometry are then applied to the *H* images to generate a comparable surface brightness profile in *H*. We found very small differences in the *H* surface brightness profile when it was determined using the *B* annuli compared to when the *H* profile was determined from an unconstrained fit to the *H* image itself. How-

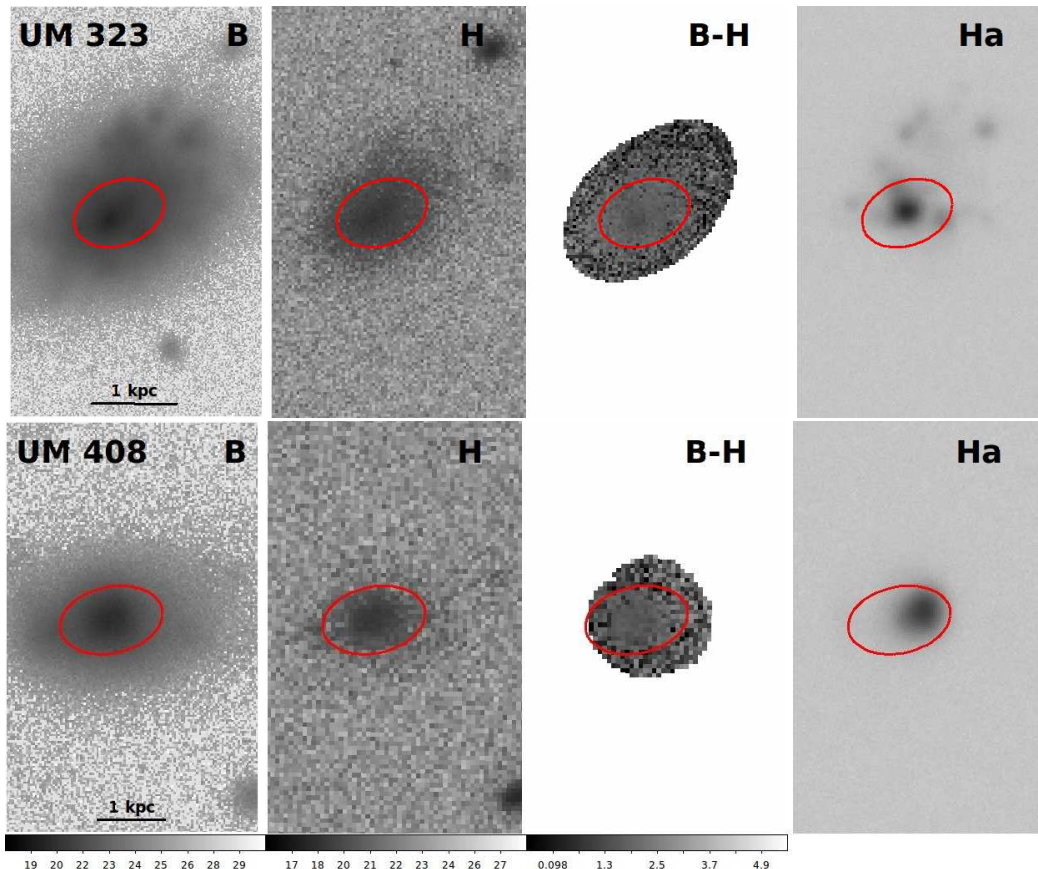


FIG. 1.— Final images of the BCDs. Shown here are the primary observations of each BCD in our sample, all matched to the  $B$  image. The left-most panel shows an inverted image in the  $B$  filter with  $0.14''$  pixels, logarithmic intensity scaling, and a scale bar 1 kiloparsec in length. The scale at the bottom shows the calibrated surface brightness in  $\text{mag}/\text{arcsec}^2$ . The left-center panel shows an inverted image in the  $H$  filter binned  $2 \times 2$  (resulting in  $0.28''$  pixels) with logarithmic intensity scaling. Again the scale at the bottom shows the calibrated surface brightness in  $\text{mag}/\text{arcsec}^2$ . The right-center panel shows a  $B-H$  color map with  $2 \times 2$  binning ( $0.28''$  pixels) where darker grey shading corresponds to bluer colors, as shown in the scale bar at the bottom. The color map is truncated beyond where the signal-to-noise of the  $B$  and  $H$  images is too low. The right-most panel shows an inverted continuum-subtracted  $H\alpha$  image with a logarithmic intensity scaling, and  $0.14''$  pixels. On all images, an ellipse marks the isophote inside of which more than half of the pixels in each isophote are masked. Inside of that ellipse, our isophotal parameters have their geometric parameters fixed.

ever, due to the shallower nature of the  $H$  images, the  $B$  annuli are able to trace the  $H$  profiles to fainter levels than if the  $H$  images had been fit with independent isophotes.

These same  $B$  annuli are also used on each of the SDSS  $ugriz$  images to determine surface brightness profiles in each filter. The use of spatially-matched images and common isophotes for all wavelengths allows us to create surface brightness profiles where each isophotal annulus measures the same physical part of the galaxy in each filter, enabling us to also create *surface color* profiles. We also apply a correction in each filter for Galactic extinction obtained through NED, from the recently recalibrated dust maps of Schlafly & Finkbeiner (2011).

Dwarf galaxy surface brightness profiles can be fit with a wide variety of functions across their radial extent. A wide variety of surface brightness profile breaks are observed in dwarf galaxies (Herrmann et al. 2013), but each component is still fitted with exponential profiles (Hunter & Elmegreen 2006), consistent with stellar disks. As motivated in Section 2.1, in order to probe the structure of the underlying old stellar populations in the outskirts of the BCDs, we fit only the outer portion of each BCD’s surface brightness profile, where the shape is well described by a single exponential profile. This exponential

decline likely indicates the presence of a somewhat regular underlying stellar disk.

The inner limit of the fit to the underlying host galaxy is set at the point where the contamination by light from recent or ongoing star formation is no longer significant and the profile has a simple exponential decline. The outer limit of the fit is set by the signal-to-noise of the profile above the sky background, in terms of how bright the galaxy is relative to the standard deviation ( $\sigma$ ) of the measured sky level. Sometimes these fit limits are different between the  $B$  and  $H$  filter, owing usually to the shallower nature of the  $H$  images. In a few cases the  $H$  images are not deep enough to reach a region where the  $H$  surface brightness profile follows an exponential decline, and no  $H$  profile fitting is possible. For this reason, we do not fit  $H$  profiles to Was 5, Mk 36, or UM 461 (c.f. Hunter & Elmegreen 2006, Lagos et al. 2011, and Micheva et al. 2013, for deeper NIR profiles).

We use the SDSS  $g$  and  $r$  profiles to construct a  $B - V$  profile with the photometric conversions from Jester et al. 2005. While the  $g$  and  $r$  images are less deep than our observations, the additional color information is valuable even if it is only available in the higher surface brightness regions of the BCDs. The  $B - V$  and  $B - H$  colors typically flatten to a constant value in the region

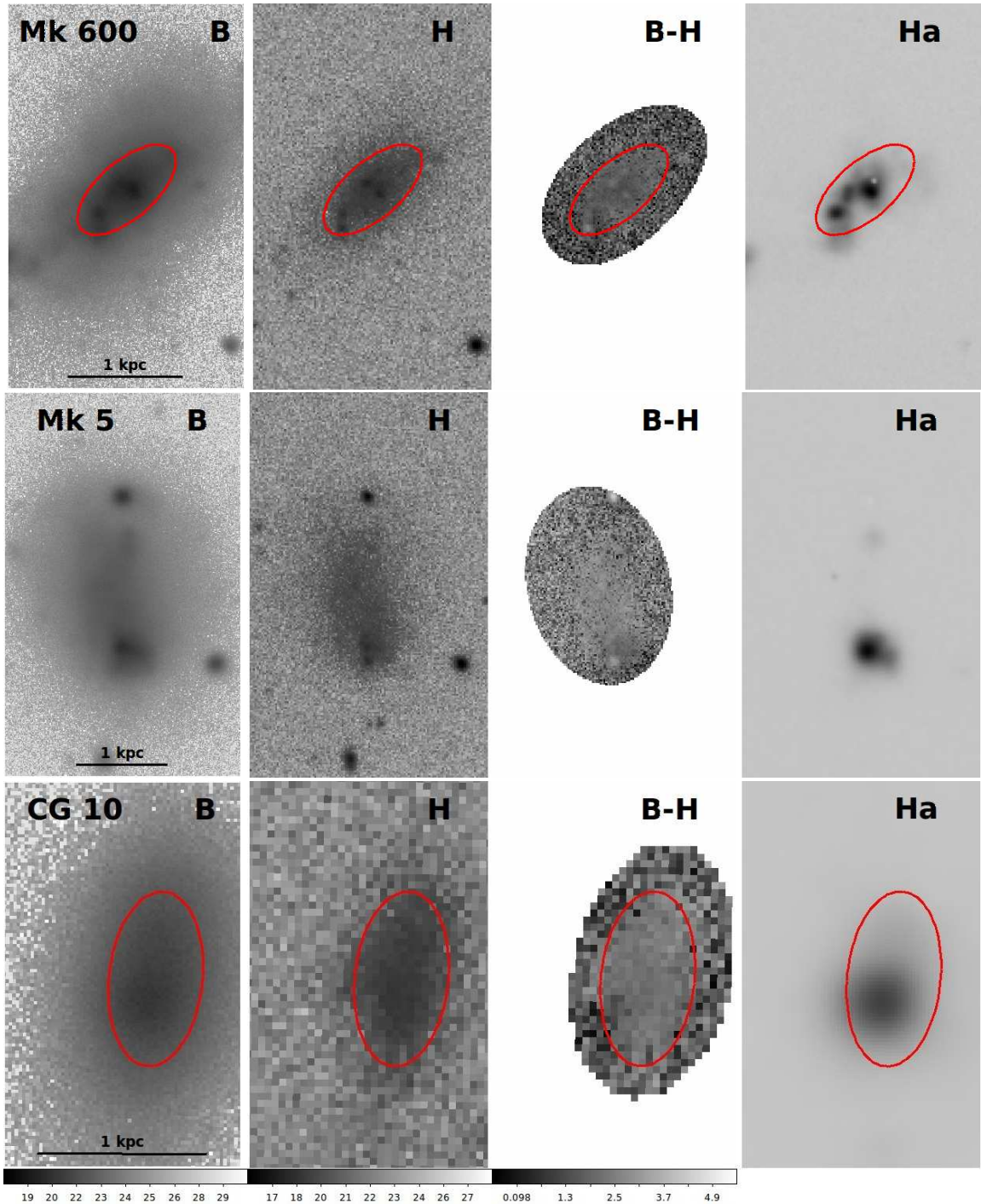


FIG. 1.— continued

of the outskirts where we fit exponentials to the profiles, and we compute the average color within this region as well.

Our linear least-squares fit to the surface brightness profiles of the underlying host galaxy gives a best-fit value of the slope (related to the disk scale length) and intercept (related to the central surface brightness), but these observed quantities must be converted to intrinsic quantities. First we need to geometrically correct the observed central surface brightness  $\mu$  to the central surface brightness for a face-on orientation  $\mu^0$  using a determination of the inclination angle,  $i$ , assuming an optically

thin disk, with:

$$\mu^0 = \mu - 2.5 \log \cos i.$$

Following the method of Staveley-Smith et al. (1992), we consider the galaxy as an oblate spheroid with thickness to length ratio  $q$ , which on average for dwarf galaxies is  $\langle q \rangle = 0.57$ . Staveley-Smith et al. (1992) derived the following relationship between semi-minor to semi-major axis ratio  $b/a$ , and the thickness-to-length ratio  $q$ :

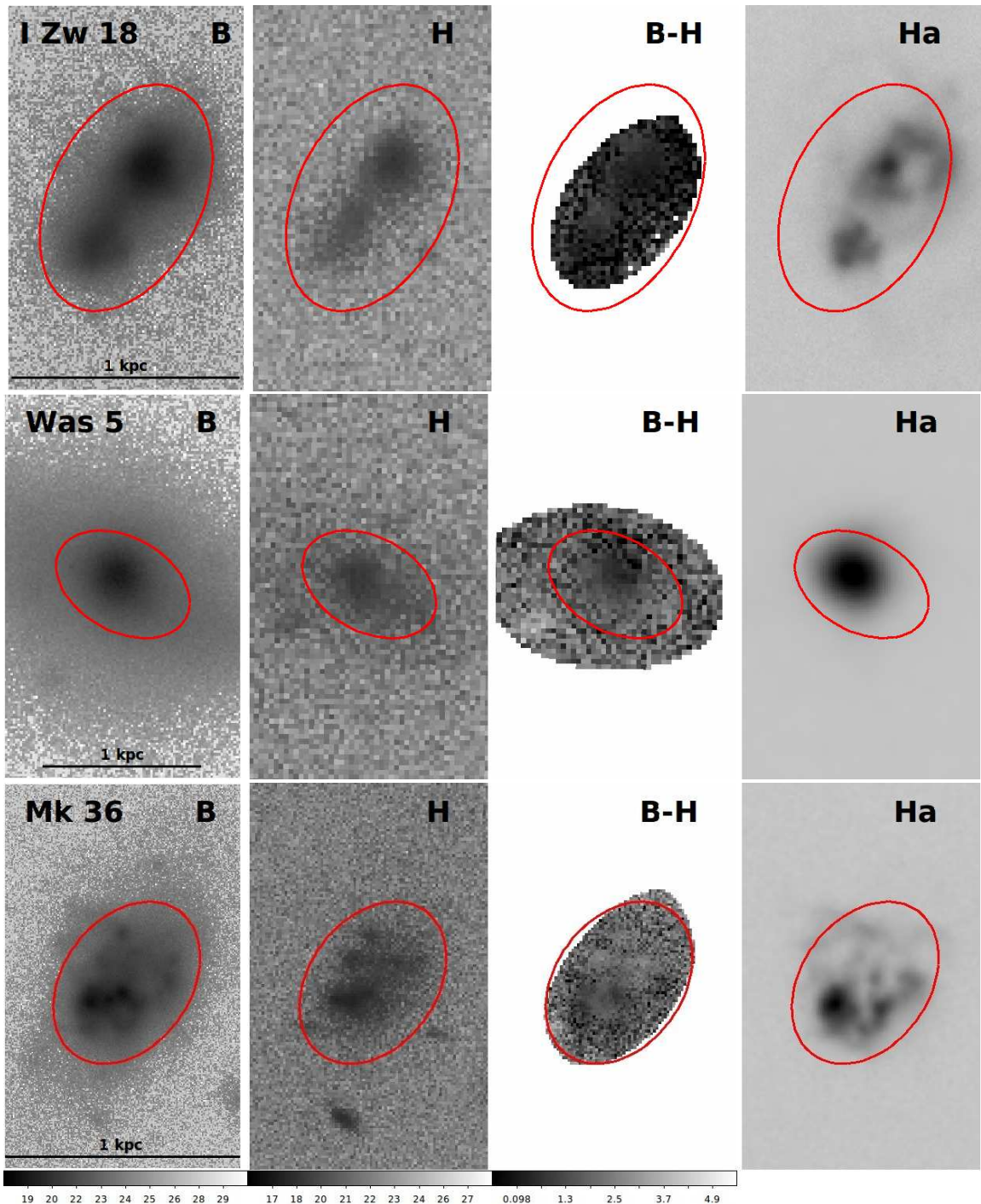


FIG. 1.— continued

$$q = 0.65(b/a) - 0.072(b/a)^{3.9}.$$

For each galaxy we determine the mean ellipticity ( $\epsilon = 1 - b/a$ ) within the outskirts of the galaxy where the underlying surface brightness profile is fit. We use this ellipticity to determine an estimate of the inclination angle, and correct all central surface brightnesses to face-on. We also use distances derived from flow models (Mould et al. 2000) to convert the scale radius into physical units. All of these best-fit parameters are listed in Table 2, and are plotted in the figures that follow (absolute magni-

tudes are corrected for Galactic extinction).

The surface brightness profiles, ellipticity profiles, color profiles, and fits are all shown in Figure 2. For each surface brightness profile we show the  $H$  and  $B$  profiles on the same scale and also plot the masked and unmasked  $B$  profile fits together to show the minimal differences. Because of the mask, the masked profile does not continue to the center of the galaxy. Instead, we show a profile of fixed-shape isophotes which takes the shape of the inner-most well-determined isophote using the mask, and extending that shape inward. Using a fixed-shape ellipse in the inner regions of the BCDs has largely a

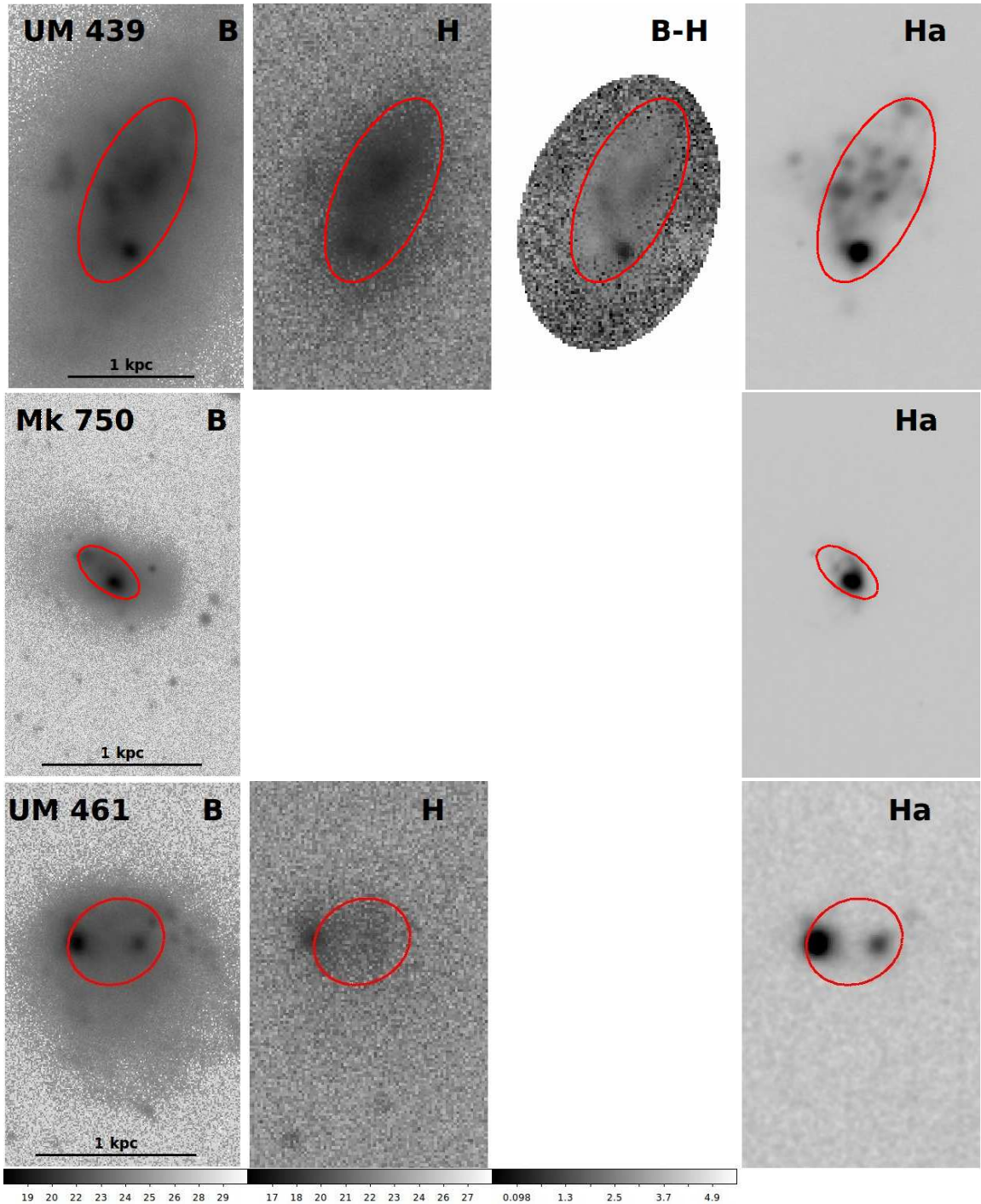


FIG. 1.— continued

cosmetic effect on the surface brightness profile, preventing the ellipse shape from varying wildly as it tries to match the irregular structures in the inner regions of most of the BCDs. The fixed-shape profile is not necessarily physically meaningful, but it is representative of the azimuthally-averaged light distribution in the complex central regions of the BCDs.

We also show the ellipticity profile at the top of each graph in Figure 2. As our profiles are all displayed in terms of semi-major axis, the ellipticity profile is necessary in order to interpret changes and shapes in the surface brightness profile. A few galaxies show dramatic

changes in ellipticity in their fits. Notably, Mk 600 has  $\epsilon \sim 0.5$  across most of its profile, but in the inner regions, the ellipticity rapidly decreases as the isophotes become much more circular. That sudden change in  $\epsilon$  causes a break in the surface brightness profile, which is evident in the graph as well. In general it is safer and simpler to use the semi-major axis for surface brightness profiles, but in cases where the ellipticity (or position angle) change rapidly, the resulting profiles are more difficult to interpret. In our BCDs, the underlying host profiles are all fit in regions of relatively stable ellipticity, so that our fits are unaffected by the irregular central regions where

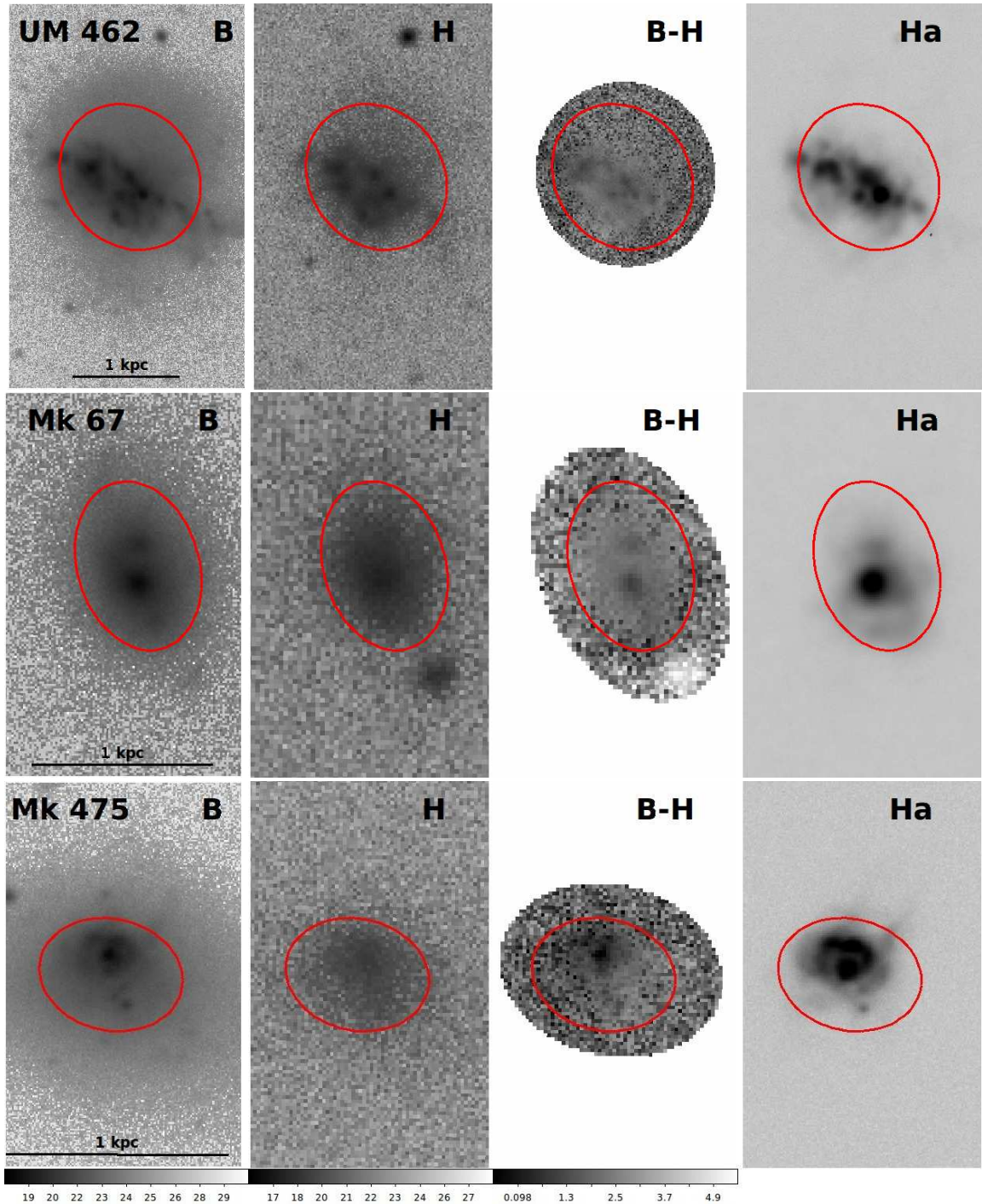


FIG. 1.— continued

isophotal shapes may change more rapidly.

The complex inner regions of the BCDs have less bearing on this work than do the outskirts, as we are most interested in the underlying host light. There are some notable shapes and features in the profiles interior to the portions we fit. Some BCDs have significant curvature in their inner profiles (Was 5, Mk 475, Mk 900, Mk 324, Mk 328), which looks similar to a deVaucouleurs profile, suggesting that these galaxies may have bulge-like centers or be similar to dEs. Other BCDs have irregular bumps and jumps in their inner profiles (Mk 5, I Zw 18, Mk 36, Mk 750), which show the difficulty of fitting smooth ellipses

to inherently more complex structures. In particular, the central regions of UM 461 and UM 462 have a bright and nearly uniform level of intensity, punctuated with sites of active star formation, which makes for a very complex environment. Finally, some BCDs have profiles which remain almost exponential over their entire extent (UM 323, UM 408, CG 10, UM 439), which may indicate a somewhat simpler recent history of star formation and activity.

The shapes of a few galaxies were particularly difficult to fit with our simple method, due to their significant irregularities. The cometary shape of Mk 5 cre-

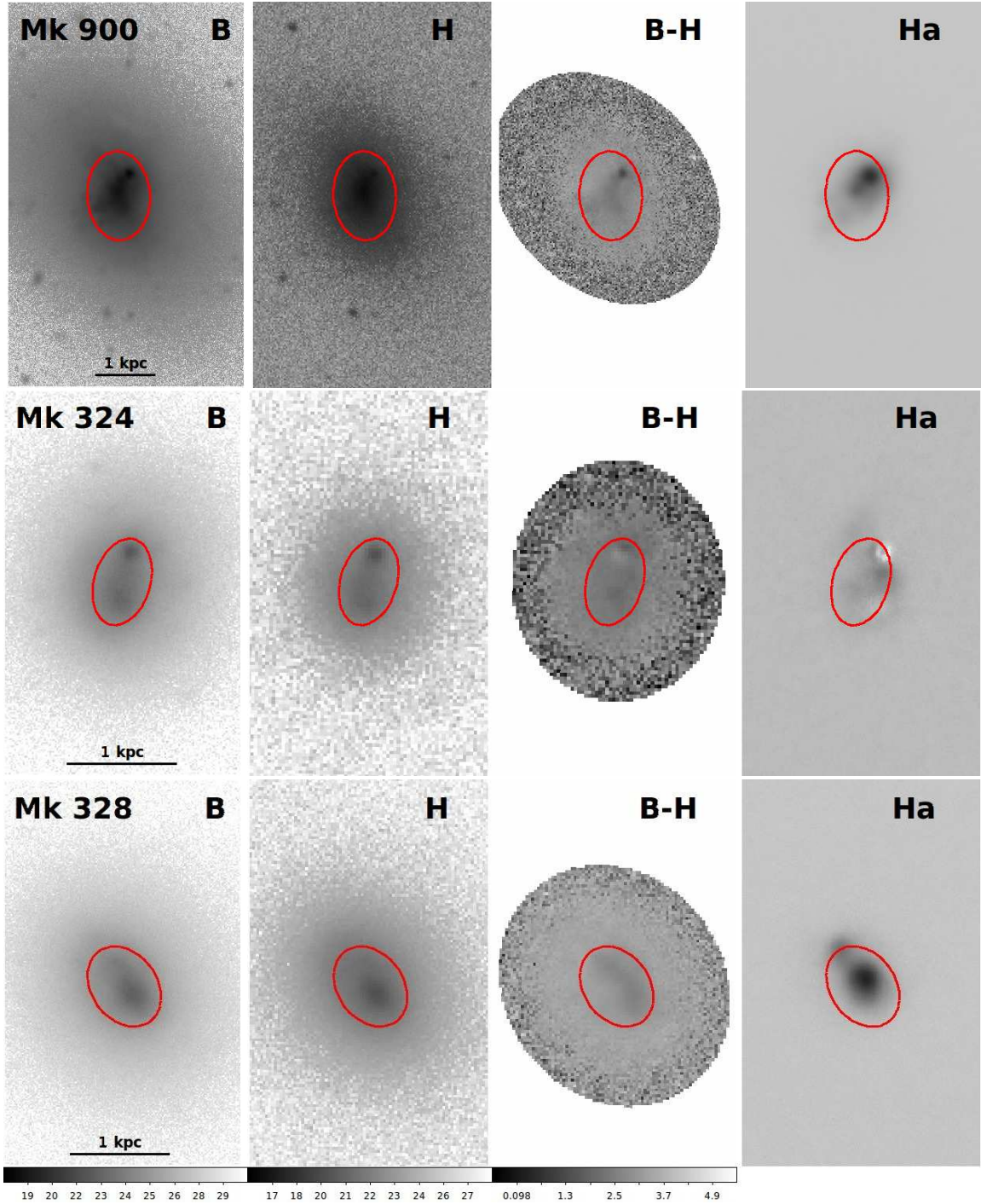


FIG. 1.— continued

ates a significant positional offset between the center of the bright star-forming region and the center of the faint outer isophotes. This rapid shifting of successive isophotes leads to a poorly determined fit in the central regions, and so we do not display the inner part of the fit. The fit to the smooth, regular outer isophotes is reliable, though, so we keep this galaxy in our sample (see also Section 6.1.1 in Amorín et al. 2007 for a 2D treatment of Mk 5). In a similar way, I Zw 18 presents a challenging structure to be fit. Because of the visible and irregular structures present throughout much of the galaxy, we caution that even though our fit is restricted to the outer-

most regions of the galaxy, we may not have reached the true underlying population of this faint, unusual galaxy.

The graphs of  $B - H$  and  $B - V$  color in Figure 2 are also powerful tools in understanding these complex galaxies. The shallower depth of the SDSS images makes the  $B - V$  profile become noisy and erratic beyond the exponential fit region. Inside the fit region and in the inner regions of the BCDs, however, the  $B - V$  and  $B - H$  profiles are mostly well behaved and have interesting features. As noted in the  $B - H$  color maps in Figure 1, the BCDs tend to have bluer centers and redder outskirts. Some BCDs have particularly strong color gradients over

most of their radial extent (CG 10, I Zw 18, Was 5, Mk 750, UM 461, Mk 67, Mk 475) while others are surprisingly flat (UM 323, UM 408, Mk 600, UM 439, Mk 324). The surface colors ( $B - V$  and  $B - H$ ), averaged within the region of the profile where we fit an exponential, are given in Table 2, and are fairly red. A more detailed analysis of both the surface colors and the color gradients throughout the BCDs is discussed in Section 4.5 and shown in Figure 6.

#### 4. RESULTS

##### 4.1. Comparison Samples

To understand where BCDs fit in the context of dwarf galaxy evolution, we select a broad set of dwarf galaxies as a comparison sample, drawn from a variety of sources in the literature. It is important that we select only studies which used similar surface brightness profile fitting methods to ours, and which had similar goals in separating the old stellar population from recent star formation, so that the structural parameters represent the underlying old stellar population.

Our primary optical comparison sample comes from Salzer & Norton (1999, SN99) who observed some of these same BCDs and also 11 dIs in  $B$  and  $H\alpha$  filters and used this same method to fit exponential profiles to the outskirts of the surface brightness profiles. We supplement these comparison dIs with other samples from the literature, each of which is briefly discussed here. Patterson & Thuan (1996, PT96) studied 51 dIs and LSBs and reported results from fits of the underlying exponential profiles in the  $B$  filter. They fit the outer portions of the profile to avoid light from star-forming regions. Van Zee (2000, Z00) observed a sample of isolated dIs in  $UBV$  and  $H\alpha$ , and we include her structural parameters from exponential disk fits to 50 galaxies. Parodi et al. (2002, P+02) used observations of many late-type dwarf galaxies to fit disk profiles in  $B$  and  $R$  filters. Out of the 72 dwarfs in the sample, we use the structural parameters from the 48 that are classified as Sm or Im. Finally, we include structural parameters of 5 dwarf LSBs from Pustilnik et al. (2011, P+11), and of 109 gas-rich field dwarfs from Pildis et al. (1997, P+97).

It is also important to find an appropriate comparison sample of near-infrared observations of dwarf galaxies. Surface photometry from deep NIR observations of dwarf galaxies is relatively rare in the literature. We use the large amalgamated sample of 66 dwarf galaxies from McCall et al. 2012. These galaxies' surface brightness profiles are fitted with hyperbolic secant (*sech*) functions instead of the exponential functions used in this work, so we carried out a simple Monte Carlo simulation to derive empirical relations between the structural parameters of these two profile types. We use the galaxies' best-fit *sech* profile parameters to generate theoretical surface brightness profiles with  $\sim 5\%$  noise, and re-fit the outskirts with exponential profiles. We recover the following relations between the exponential parameters ( $\mu_{0,exp}, \alpha_{exp}$ ) and the *sech* parameters ( $\mu_{0,sech}, \alpha_{sech}$ ), where  $\mu_0$  is in  $\text{mag}/\text{arcsec}^2$  and  $\alpha$  is in parsecs:

$$\mu_{0,exp} = (0.996 \pm 0.001) * \mu_{0,sech} + (0.821 \pm 0.012)$$

$$\alpha_{exp} = (0.987 \pm 0.000) * \alpha_{sech} + (6.763 \pm 0.283)$$

Overall these fits show that it is possible to make a reliable conversion between exponential and *sech* fits. The

slopes of the relations are nearly unity, indicating no difference in the relationships across the relevant parameter space. The offset of  $\sim 0.8 \text{ mag}/\text{arcsec}^2$  in surface brightness is expected, as the *sech* profile flattens out in its central regions significantly more than the exponential profile. When plotted logarithmically, the *sech* and exponential profiles overlap at large radii, but at smaller radii the *sech* profile becomes increasingly fainter than the exponential profile. The overall rms scatter in the relation for  $\mu_0$  is  $0.06 \text{ mag}/\text{arcsec}^2$ , and in the relation for  $\alpha$  is 7.9 pc. These conversions are robust enough for this sample to be a useful comparison data set for the structural parameters of the BCDs.

From this data set, we also correct the observed central surface brightnesses to be face-on ( $\mu_0^f$ ) using the inclination angle given by McCall et al. (2012). Finally, since observations are in  $K_s$ , we determine the  $H$  filter equivalent of the the central surface brightness and absolute magnitude using a color of  $H - K = 0.1$ , which is representative of these dwarf galaxies. We also use the recent NIR observations from Noeske et al. (2005) who measured optical and NIR structural parameters for a sample of 11 BCDs, 3 of which are common to our sample.

##### 4.2. Optical Structural Parameters

We now consider relationships between the structural parameters and total luminosities of the BCD hosts relative to our comparison sample of dIs. Here the structural parameters are determined in the outskirts of the BCDs and reflect the structure of the underlying host galaxy, while the absolute magnitudes are total magnitudes for the BCDs, including both host and starburst light. The exponential fit to this underlying host galaxy has two parameters:  $\alpha$ , the scale length in kiloparsecs, and  $\mu_0$ , the central surface brightness corrected to face-on in magnitudes per square arcsecond. These structural parameters only apply to the surface brightness profile in the outskirts, and are different from the scale length of the overall galaxy light profile and the central surface brightness that the overall profile reaches at the center of the galaxy. We use  $\alpha$  and  $\mu_0$  as measures of the overall shape and structure of the underlying host galaxy, and measure them on the  $B$  image ( $\alpha_B$  and  $\mu_{0,B}$ ) and on the  $H$  image ( $\alpha_H$  and  $\mu_{0,H}$ ).

Figure 3 shows the relationship for our BCDs and comparison sample galaxies between the optical structural parameters  $\alpha_B$  and  $\mu_{0,B}$  and the  $B$  luminosity,  $M_B$ . Many groups have used these types of graphs to study the structural parameters of a wide variety of galaxies since these were first introduced (Kormendy 1977). Graham (2013) summarizes the historical and modern scaling relations for a variety of galaxies, and describes these two relationships in particular.

The relationship between scale length and luminosity is not a simple power law across the wide range of galaxy masses from dwarf to giant (Binggeli et al. 1984), but when considering samples restricted to dwarf galaxies, the relationship is well fit with a power law (Lisker 2009 for dEs, Sharina et al. 2013 for dIs). Our plot of  $\alpha_B$  vs  $M_B$  shows a clear trend for the more luminous comparison dwarf galaxies to have larger scale radii. The underlying host galaxies of the BCDs have scale radii which are unusually small for their luminosities, and seem to oc-

TABLE 2  
STRUCTURAL PARAMETERS OF UNDERLYING HOST GALAXIES OF BCDs

Galaxy	$M_{B,tot}$ [mag]	$\mu_{B,0}^0$ [mag/arcsec <sup>2</sup> ]	$\alpha_{B,exp}$ [kpc]	$M_{H,tot}$ [mag]	$\mu_{H,0}^0$ [mag/arcsec <sup>2</sup> ]	$\alpha_{H,exp}$ [kpc]	b/a	<B-V> (env.)	<B-H> (env.)
UM323	-16.10	19.85	0.30	-17.90	18.49	0.41	0.69	0.44	2.09
UM408	-16.04	20.40	0.36	-17.72	19.28	0.49	0.65	0.46	1.96
Mk600	-15.55	20.96	0.38	-17.30	18.84	0.35	0.48	0.46	1.83
Mk5	-15.18	19.79	0.25	-17.74	17.64	0.31	0.59	—	2.76
CG10	-15.01	20.10	0.23	-17.47	18.11	0.27	0.58	0.47	2.36
IZw18	-14.68	19.25	0.10	-15.19	17.31	0.10	0.66	0.45	0.97
Was5	-15.05	20.16	0.22	-16.86	—	—	0.68	0.62	2.65
Mk36	-14.23	22.17	0.22	-16.03	—	—	0.62	0.65	3.03
UM439	-16.11	20.73	0.43	-18.23	17.84	0.32	0.58	0.46	2.27
Mk750	-13.42	21.20	0.12	—	—	—	0.61	0.61	—
UM461	-14.40	21.28	0.17	-15.87	—	—	0.88	0.41	1.44
UM462	-16.18	20.25	0.24	-18.07	17.95	0.24	0.89	0.45	2.42
Mk67	-15.16	20.16	0.17	-17.42	19.52	0.63	0.70	0.54	2.71
Mk475	-14.28	22.16	0.24	-16.25	20.04	0.33	0.74	0.56	2.65
Mk900	-17.16	21.45	0.73	-19.85	18.32	0.70	0.72	0.80	3.12
Mk324	-16.70	20.40	0.28	-19.08	17.76	0.27	0.85	0.65	2.65
Mk328	-16.57	21.37	0.39	-19.57	17.81	0.37	0.85	0.90	3.34

NOTE. — Our H observations of Was 5, Mk 36, and UM 461 were not sensitive enough for surface brightness profile fitting. The  $b/a$  values are averages determined for the underlying host galaxy, within the same range of SMA as the exponential fit.

occupy one edge of the parameter space defined by the comparison galaxies. In fact, the underlying host galaxies of the BCDs are displaced from the comparison sample in the sense that they have smaller scale lengths for their luminosity, which, assuming an exponential disk profile, implies they will also have brighter central surface brightnesses. The left panel of Figure 3 also includes a dashed line showing the relationship between  $\alpha_B$  and  $M_B$  for an exponential profile with  $\mu_{0,B} = 25$  mag/arcsec<sup>2</sup>. This central surface brightness is typical for very low surface brightness galaxies, and as they are difficult to observe, the comparison sample contains very few galaxies in this region. The underlying host galaxies of the BCDs are found on the opposite side of this parameter space, indicating that they have exceptionally bright central surface brightness.

The relationship between luminosity and central surface brightness has been characterized with a single power law from  $-12 > M_B > -20$  (Binggeli et al. 1984, Binggeli & Cameron 1991), but appears to deviate brighter than  $M_B \sim -20$ . Our relationship between  $\mu_{0,B}$  and  $M_B$  for the comparison dwarf galaxies shows a large scatter across much of parameter space. Even so, the underlying host galaxies of the BCDs have central surface brightnesses which are at and beyond the bright edge of the parameter space defined by the comparison galaxies. As with the scale length relationship, there are implicit restrictions on this parameter space. To show these limits, the right panel of Figure 3 includes lines indicating the relationships for exponential disks with particular scale lengths. The comparison sample does not include more than a few galaxies with scale lengths smaller than  $\alpha_B \sim 150$  pc, as systems much smaller than that are not likely to be classified as galaxies. Here again, the underlying host galaxies of the BCDs are near the edge of parameter space with their unusually bright central surface brightnesses and small scale lengths.

Both of these relationships for the underlying host galaxies of BCDs have been discussed previously in great detail, but never with as simple and direct a method as

we employ. Even with the variety of analysis and fitting methods used, previous works have reached similar conclusions to those of this work (Papaderos et al. 1996, Amorín et al. 2009, Gil de Paz & Madore 2005). In particular, Papaderos et al. (1996) found that BCD hosts have  $\mu_{0,B}$  enhanced by  $\sim 1.5$  mag and have  $\alpha_B$  which are a factor of  $\sim 2$  smaller than comparison dIs of similar  $M_B$ . Our comparison sample of dIs in the same luminosity range as the BCDs ( $M_B = -17$  to  $M_B = -14$ ) has a median  $\mu_{0,B} = 22.85$  mag/arcsec<sup>2</sup> with a standard deviation of 1.03 mag/arcsec<sup>2</sup>. The underlying hosts of our BCD sample have a median that is nearly 2.5 magnitudes brighter, at  $\mu_{0,B} = 20.40$  mag/arcsec<sup>2</sup> with a standard deviation of 0.83 mag/arcsec<sup>2</sup>. In terms of scale length, our luminosity-matched comparison sample has a median  $\alpha = 1.01$  kpc with a standard deviation of 0.68 kpc, while the BCD hosts in our sample have a median  $\alpha = 0.24$  kpc, with standard deviation 0.15 kpc. However, these median statistics are only intended to roughly quantify the significant differences between the structure of the BCD hosts and the structure of the comparison galaxies. As is apparent from Figure 3, there is a broad and continuous distribution of structural parameters with a wide variety of values for dwarf galaxies. The structural parameters of the BCD hosts are distinctly at one extreme of this continuum.

We also indicate in Figure 3 the comparison galaxies that have similar structural parameters to the underlying host galaxies of the BCDs. These “BCD-like” comparison galaxies have structural parameters within  $1\sigma$  of the locus of BCD host points on each graph, and we find 9 of them, as listed in Table 3. While a detailed followup of these galaxies is outside the scope of this work, we do note that they typically have blue colors consistent with star forming dIs (van Zee 2001). These galaxies could represent candidates for post- or pre-burst BCDs, which are not currently experiencing an intense starburst, but which still have the unusually concentrated underlying stellar distribution. In this way, morphology alone is not enough to classify a dwarf galaxy as a BCD or as a dI.

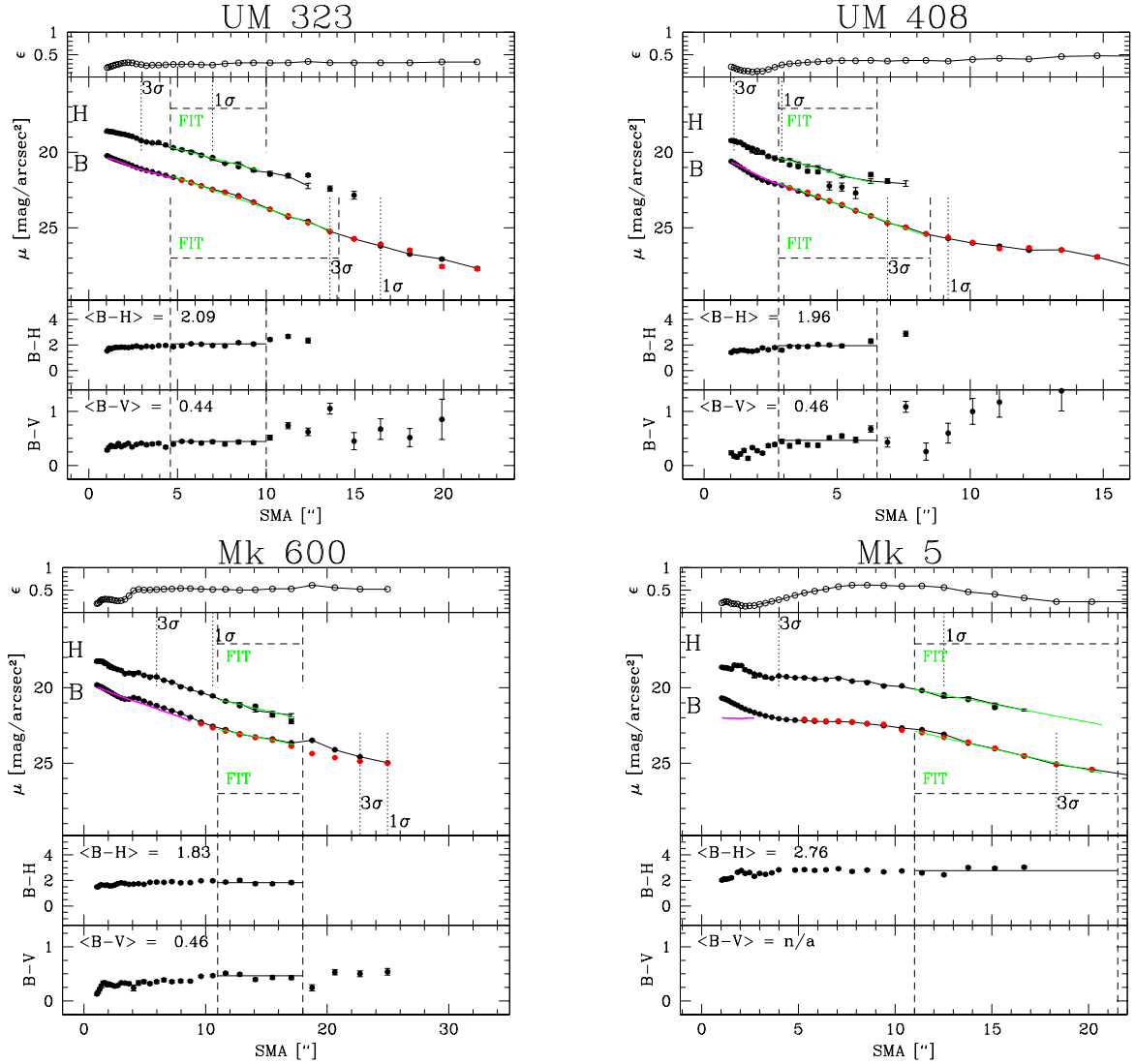


FIG. 2.— Surface brightness profiles and fits. Each graph shows the surface brightness profiles, color profiles, and fits for each BCD, plotted as a function of semi-major axis (SMA), in arcseconds. The large main panel shows the unmasked  $B$  surface brightness profile (connected black dots), the masked  $B$  surface brightness profile (red dots), the inner region of fixed-shape fit (magenta line), the  $H$  surface brightness profile from an unconstrained fit (black dots), and the  $H$  surface brightness profile as constructed from the best-fitting  $B$  ellipses (black line). Vertical dotted lines show the thresholds where the surface brightness profiles reach  $3\sigma_{sky}$  and  $1\sigma_{sky}$ , and connected vertical dashed lines show the SMA range used to fit the profile. The exponential fits to the underlying host galaxies are shown as green lines, over the range of SMA where they were determined. The upper panel shows the ellipticity of the best-fit unmasked isophotes as a function of SMA. The lower middle panel shows the  $B-H$  profile as calculated within the matched ellipses between the  $B$  and  $H$  images, and the average  $B-H$  color within the common fit region from both filters. The bottom panel shows the  $B-V$  color as converted from the matched  $g$  and  $r$  profiles (see Section 3).

TABLE 3  
BCD-LIKE COMPARISON GALAXIES

ID	$M_B$ [mag]	$\alpha_B$ [kpc]	$\mu_{0,B}$ [mag/arcsec <sup>2</sup> ]	Reference
UGC 1104	-16.08	21.06	0.44	Z00
CGCG 007-025	-15.75	20.53	0.37	Z00
UGC 5288	-14.44	20.57	0.23	Z00
UGCA 439	-16.73	19.74	0.30	Z00
UGC 2905	-14.41	21.30	0.22	P02
NGC 2915	-16.61	21.26	0.50	P02
UGC 00772	-16.65	21.29	0.47	PT
UGC 03860	-18.72	19.67	0.60	PT
D640-15	-19.09	20.43	1.60	P+97

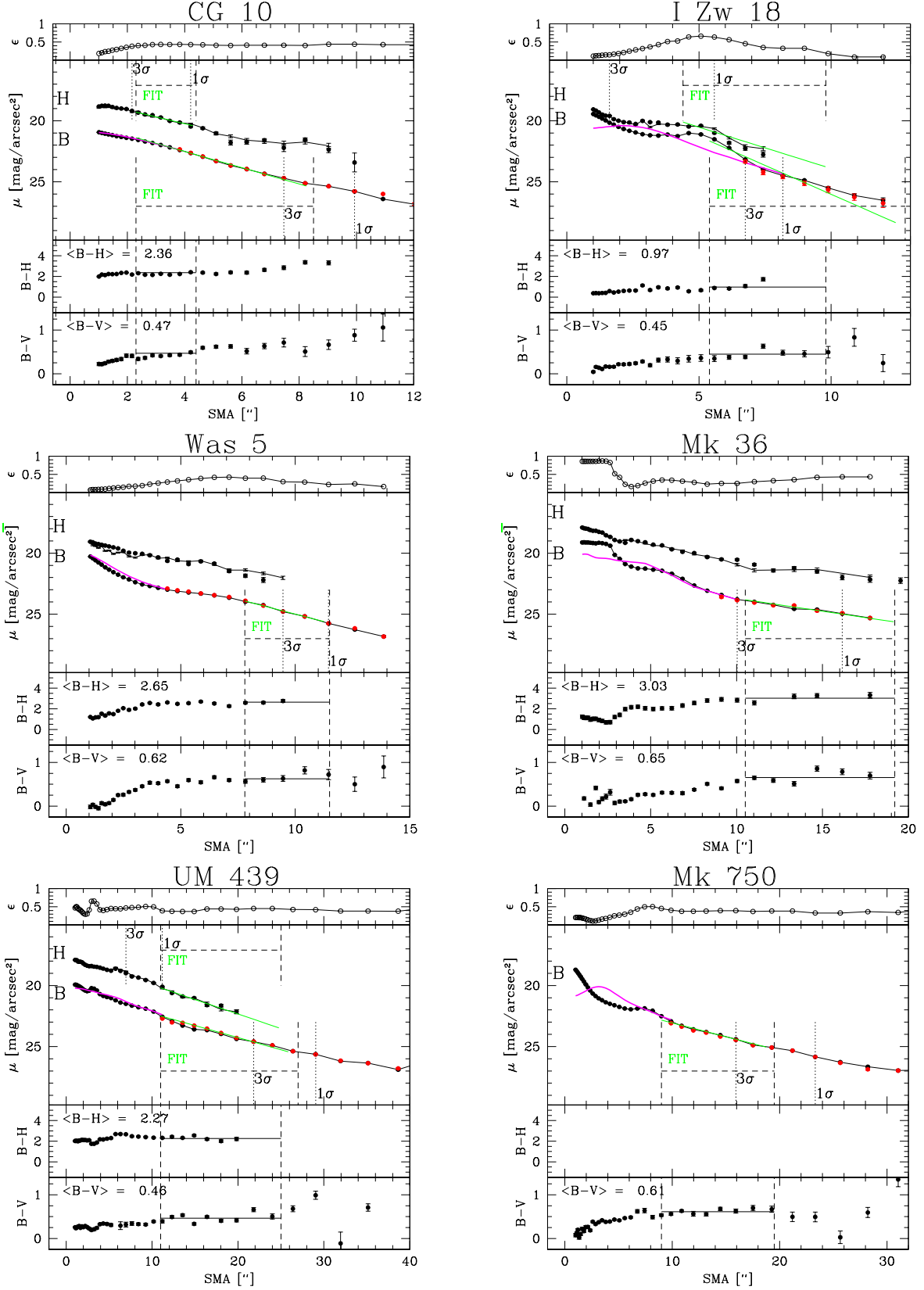


FIG. 2.— continued

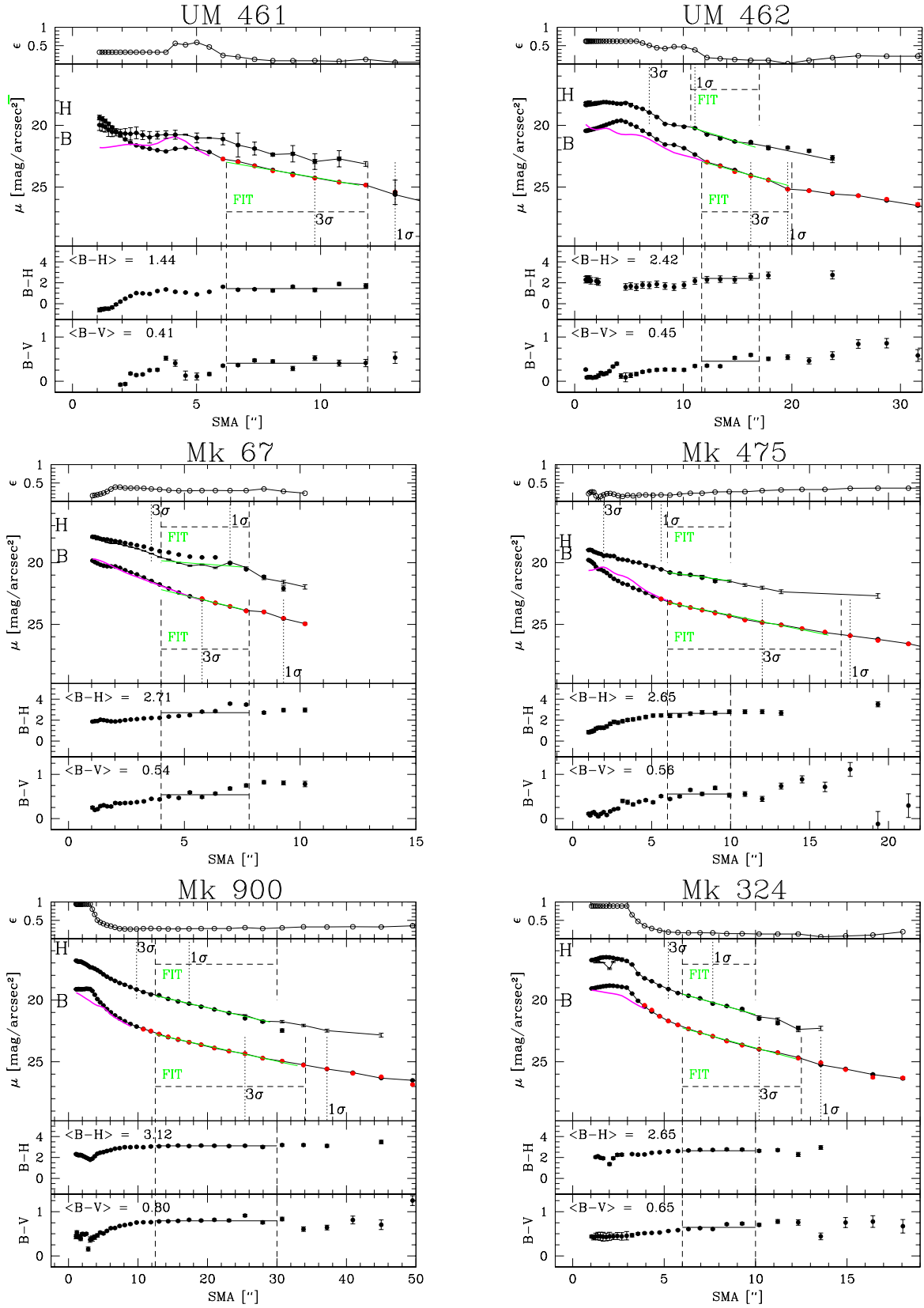


FIG. 2.— continued

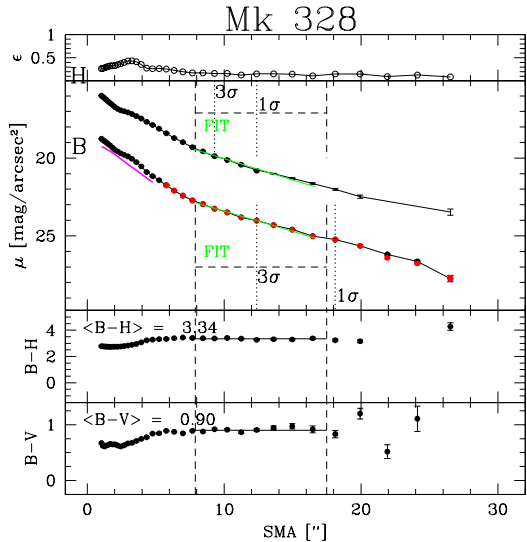


FIG. 2.— continued

Without considering the compactness of the underlying light distribution, some BCDs may be classified as dIs and some dIs may be classified as BCDs. It may be that a concentrated underlying host is a necessary requirement for a galaxy to become a BCD, and the concentrated distribution may persist after the BCD starburst has aged and faded.

#### 4.3. Near-infrared Structural Parameters

Next we look at the relationships between the NIR structural parameters ( $\alpha_H$  and  $\mu_{0,H}$ ) and the overall  $H$  luminosity,  $M_H$ . Figure 4 shows these relationships for our BCDs and comparison samples. The trends with NIR structural parameters are similar to those seen in the optical structural parameters. The dIs form a sequence in their NIR structural parameters such that BCDs at a given absolute  $H$  magnitude typically have smaller  $\alpha_H$  than the comparison sample, although the slope is shallower than it was for the  $\alpha_B$  relationship. The  $\mu_{0,H}$  of the dIs also gets fainter for fainter absolute  $H$  magnitudes, but with a stronger trend than for the  $\mu_{0,B}$  relationship. In both plots the BCD sample (both ours and those of Noeske et al. 2003) exists at an extreme of parameter space. Just as seen with  $\alpha_B$ , the BCD hosts have smaller  $\alpha_H$  for a given  $M_B$  than the dIs, and the BCD hosts have brighter  $\mu_{0,H}$  than the dIs. Even within the broad continuum of NIR structural parameters, the BCD hosts are exceptionally compact.

#### 4.4. Optical and Infrared Structural Parameters

In order to more directly probe the relationship between structural parameters and stellar mass of the underlying hosts of BCDs, we consider the aperture magnitudes from the WISE catalog of photometry (Wright et al. 2010), for all of our BCD sample and comparison sample. In Figure 5, we show the relationship between the  $B$  structural parameters ( $\alpha_B$  and  $\mu_{0,B}$ ) and the absolute luminosity in the  $w1$  band of WISE. Not all of the comparison sample dIs have been measured in WISE, owing to their apparent faintness. For those galaxies which were well-measured by WISE, we determined their absolute magnitude in  $w1$  with the same distance used to

determine  $M_B$ . The two graphs shown in Figure 5 are analogous to the optical structural parameters shown in Figure 3, but now we use  $w1$  instead of  $M_B$ . The  $w1$  filter, at  $3.4\mu\text{m}$ , is more directly measuring the stellar mass, while the  $B$  filter measurement can be significantly affected by the starbursts in the BCDs.

It is important to note that the trends apparent in the graphs of optical structural parameters persist into the graphs with  $w1$  luminosities. In fact, the trends may even be stronger when measured this way. In the relationship between  $\alpha_B$  and luminosity, when we plot versus  $w1$ , the BCDs actually move further away from the comparison sample than they were in  $M_B$ . When plotted in terms of  $M_B$ , at a given scale length, a BCD host is on average  $\sim 3$  mag brighter than a dI galaxy. This offset increases to an average separation of  $\sim 4$  mag when considering  $w1$  instead of  $M_B$ . In the relationship between  $\mu_{0,B}$  and luminosity, the change from  $M_B$  to  $w1$  does not significantly change the position of the BCD hosts relative to the dIs. The BCD hosts already had significantly higher central surface brightnesses than the dIs, and no luminosity shift can alter that. Overall, since the infrared luminosity makes the BCD hosts even more distinct, we can be sure that the unusual structural parameters of the BCDs are not just a result of their current bursts of star formation. It is clear that the underlying old stellar host is fundamentally different in BCDs.

#### 4.5. Color-color profiles

We use the matched color profiles shown previously in Figure 2 to construct a modified surface color-color diagram shown in Figure 6. We divide our BCD sample into groups based on their metallicity, and show the galaxies with metallicities  $Z \approx 7.23$  in the top two panels: those with  $Z \approx 8.23$  in the bottom left panel, and those with  $Z \approx 8.53$  in the bottom right panel. For each galaxy we first plot a triangle at the  $B-H$  and  $B-V$  colors of its radial brightness profile at one half of the effective radius. Next we plot the colors at one effective radius, two effective radii, and so on, until we reach the region where the underlying host profile is being fit. The final square point for each galaxy shows the average  $B-H$  and  $B-V$  colors of the outer envelope where we are fitting the structure of the underlying host galaxy. The error bars on the final point show the standard deviation of all isophotes within the region where the exponential profile is fit. We do not plot the central surface color since the  $B$ ,  $H$ , and SDSS images often have incompatible spatial resolutions.

Also shown are evolutionary tracks from Simple Stellar Population (SSP) models (Bressan et al. 2012, Girardi et al. 2010, obtained at: <http://stev.oapd.inaf.it/cmd>). The Bressan et al. (2012) models do not include contributions from Thermally-Pulsating Asymptotic Giant Branch (TP-AGB) stars, while the Girardi et al. (2010) models do include TP-AGB stars. Models are generated at metallicities that match the gas-phase abundances of the BCDs and are shown in the appropriate panels. These  $B-V$  vs  $B-H$  evolutionary tracks do not include any non-stellar effects in the light output of the BCDs, such as dust absorption, hot dust emission, nebular emission lines, nebular continuum, etc. While dust can have significant effects on galaxy colors, the low metallicities

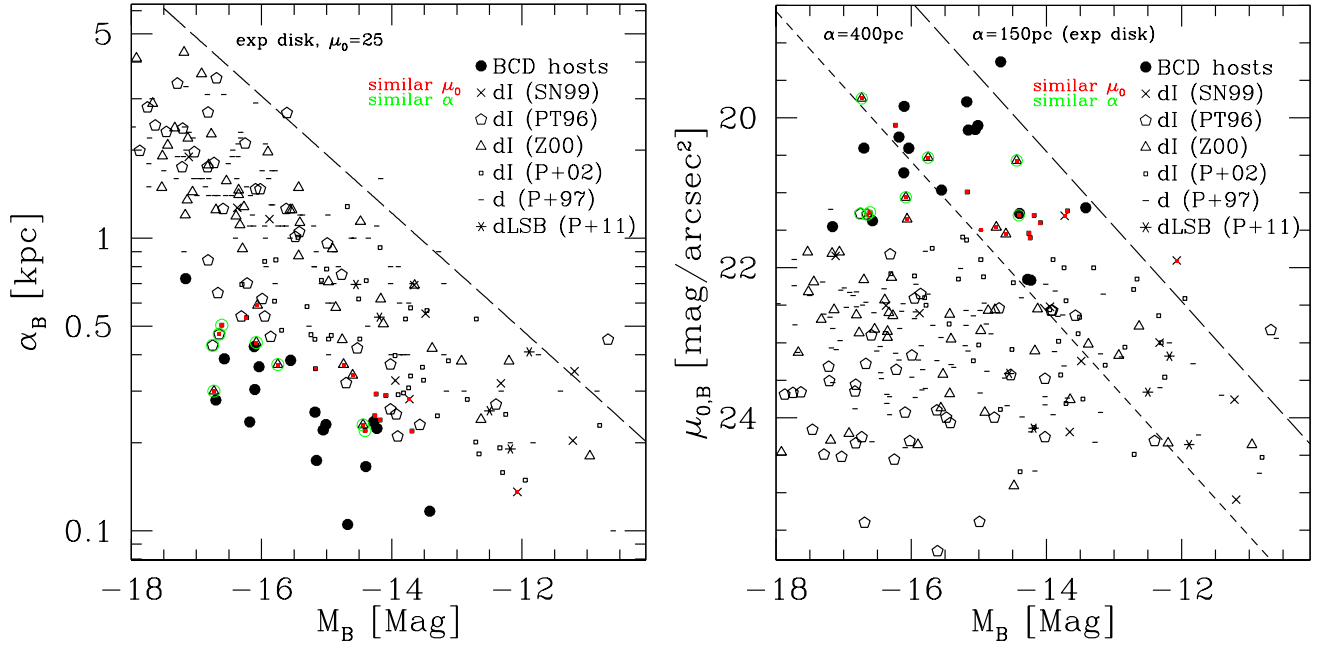


FIG. 3.— Optical structural parameters ( $B$  scale length  $\alpha_B$  and central surface brightness  $\mu_{0,B}$ ) as a function of  $M_B$  for the underlying host galaxies of BCDs and the comparison samples. We highlight the comparison galaxies which have similar  $\alpha_B$  and similar  $\mu_0$  to the BCD hosts with an open green circle if they have similar scale lengths, and an internal red dot if they have similar central surface brightnesses. Diagonal lines indicate the relationships between parameters for exponential disks with the given parameters. On the left panel, the long-dashed line shows the relationship between  $\alpha_B$  and  $M_B$  for a pure exponential disk with  $\mu_{0,B} = 25$  mag/arcsec<sup>2</sup>. On the right panel, the long-dashed line shows the relationship between  $\mu_{0,B}$  and  $M_B$  for a pure exponential disk with  $\alpha_B = 150$  pc, and the short-dashed line shows an exponential disk with  $\alpha_B = 400$  pc.

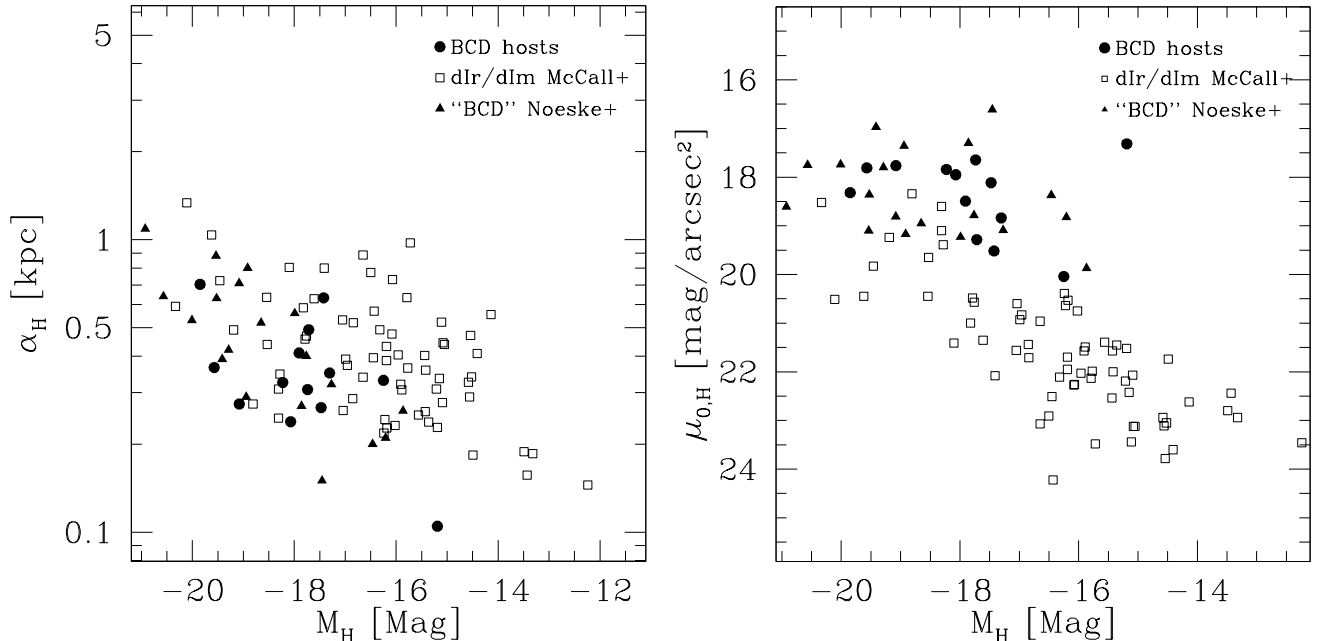


FIG. 4.— NIR structural parameters ( $H$  scale length  $\alpha_H$  and central surface brightness  $\mu_{0,H}$ ) as a function of  $M_B$  for the underlying host galaxies of the BCDs and the comparison samples.

of these systems suggest that they will not have very much dust. Most of our BCDs have strong emission lines (notably  $H\alpha$ , but also [OIII] 5007 and others), which may affect the broadband colors particularly in their inner regions. Emission-line contamination should be negligible in the underlying host colors as measured in the outermost isophotes. We take these SSP model tracks as representative of stellar evolution in these

systems, but do not expect exact agreement with our observations.

The BCDs show colors indicative of younger stellar populations near their centers, and colors consistent with older populations in their outskirts. This old population in the outskirts has been identified earlier, but is confirmed more robustly with this comparison to actual SSP models, even though these simple models do not include

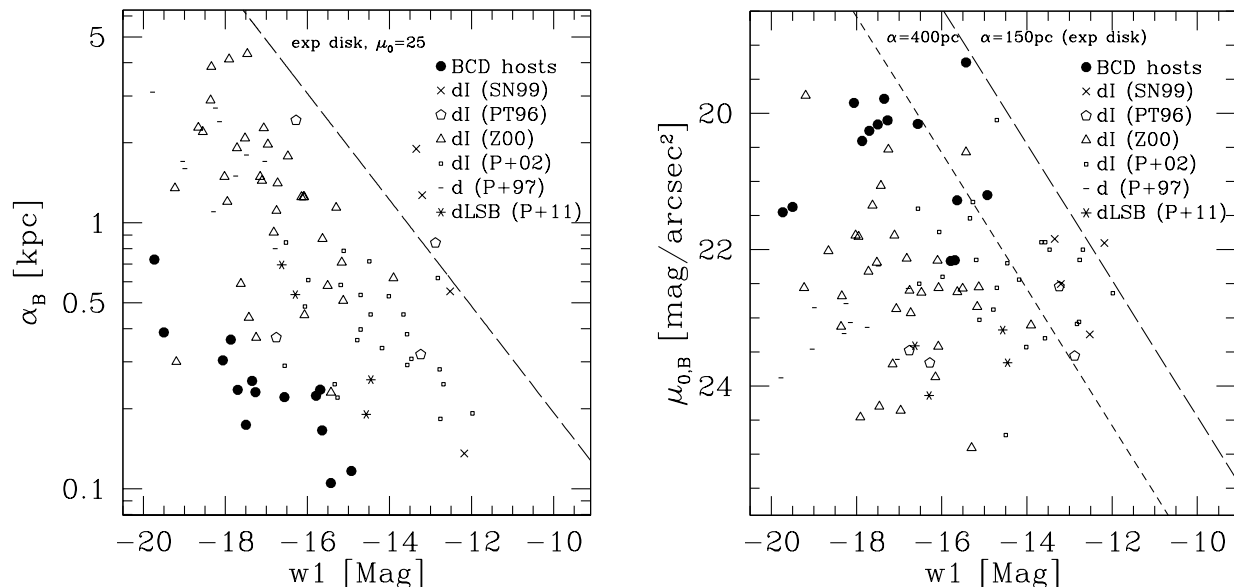


FIG. 5.— Optical structural parameters ( $B$  scale length  $\alpha_B$  and central surface brightness  $\mu_{0,B}$ ) as a function of  $M_{w1}$  for the underlying host galaxies of BCDs and the comparison samples. Diagonal lines indicate the relationships between parameters for exponential disks (of color  $B - H = 0$ ) with the given parameters.

non-stellar emission or absorption. The paths that individual BCDs take in color-color space all show radial age gradients in the sense that the average age of the stellar population increases with increasing radius throughout the BCD. This radial increase in average stellar age is seen all the way to the outskirts of the BCDs, which gives some constraints on the formation and evolution of these galaxies. This universal age gradient might suggest that new stars are formed in the (often irregular) inner regions of BCDs, and gradually diffuse into the outskirts over time. Alternatively, this age gradient could mean that  $\sim 10^{9.5}$  years ago (the typical age of the outskirts), star formation took place across the entire BCD, and gradually became more confined to the central regions like it is today, perhaps as gas outflows quenched the ongoing star formation. It is also possible that most of the evolved stars were formed in an early star formation event and the younger average ages near the center are a result of recurrent starburst events producing young stars. Still, even at  $0.5 r_{eff}$ , the color-color diagram indicates relatively old average ages for the BCDs: the youngest, Mk 475, is around  $10^8$  yr, but most are around  $10^{8.5} - 10^9$  yr. This underlying population age is in stark contrast with the ages of the most recent star formation, and it is important to note that there appears to be a significant presence of evolved stars even near the actively star-forming regions of these BCDs. The central regions of all the BCDs have significant  $H\alpha$  emission, which means O and B stars must be present to ionize the neutral hydrogen gas. Those O and B stars only live 30 Myr or less, so the central star formation is indeed very recent. However, it is an open question whether or not the current burst of star formation will create enough new young stars to significantly lower the average age of the outer regions of the BCDs.

#### 4.6. Burst Strength

In order to quantify the significance of the current star formation event, we calculate the burst strength parameter for our BCDs. Burst strength is usually parametrized

in terms of luminosity, and is the ratio between the light coming from the recently formed stars and the overall total luminosity of the galaxy. In the simplest scenario, the underlying host galaxy light is well-described by an exponential profile, while the starburst is simply an addition of light near the center. It is more complex to determine the burst strength in real galaxies. Salzer & Norton (1999) observed a similar sample of BCDs and dIs, and derived surface brightness profiles for both galaxy types. In the same manner as this study, they fit the underlying host galaxy light with exponential profiles, and integrated those fits to derive total luminosities of the underlying host. However, as many groups have noted (e.g. McCall et al. 2012), the surface brightness profiles of dIs tend to flatten near their centers, so the extrapolation of the exponential profile tends to overestimate the observed central surface brightness. In typical non-starbursting dIs, the integrated luminosity of the exponential fit to the host is on average  $\sim 0.7$  mag brighter than the total observed luminosity of the galaxy (Salzer & Norton 1999). To meaningfully determine burst strength in our sample of BCDs, we must remove this average offset to correct the burst strength to its true value. In fact, we find that in many cases, an extrapolation the exponential fits of the underlying hosts of the BCDs would predict a brighter central surface brightness than the observed value. Just as we parametrize both the dIs and BCD hosts with a single exponential function, we assume both will follow the same functional form. Even though the BCD hosts typically have shorter exponential scale lengths than dIs of similar luminosity, we expect them both to similarly flatten in their centers. In this way, our determination of the corrected burst strength of the BCDs will represent the excess luminosity contributed by the starburst, without being affected by the centrally-flattening surface brightness profile of the underlying host.

Following this method, we integrate the exponential profile fits to the underlying hosts of our BCDs and ap-

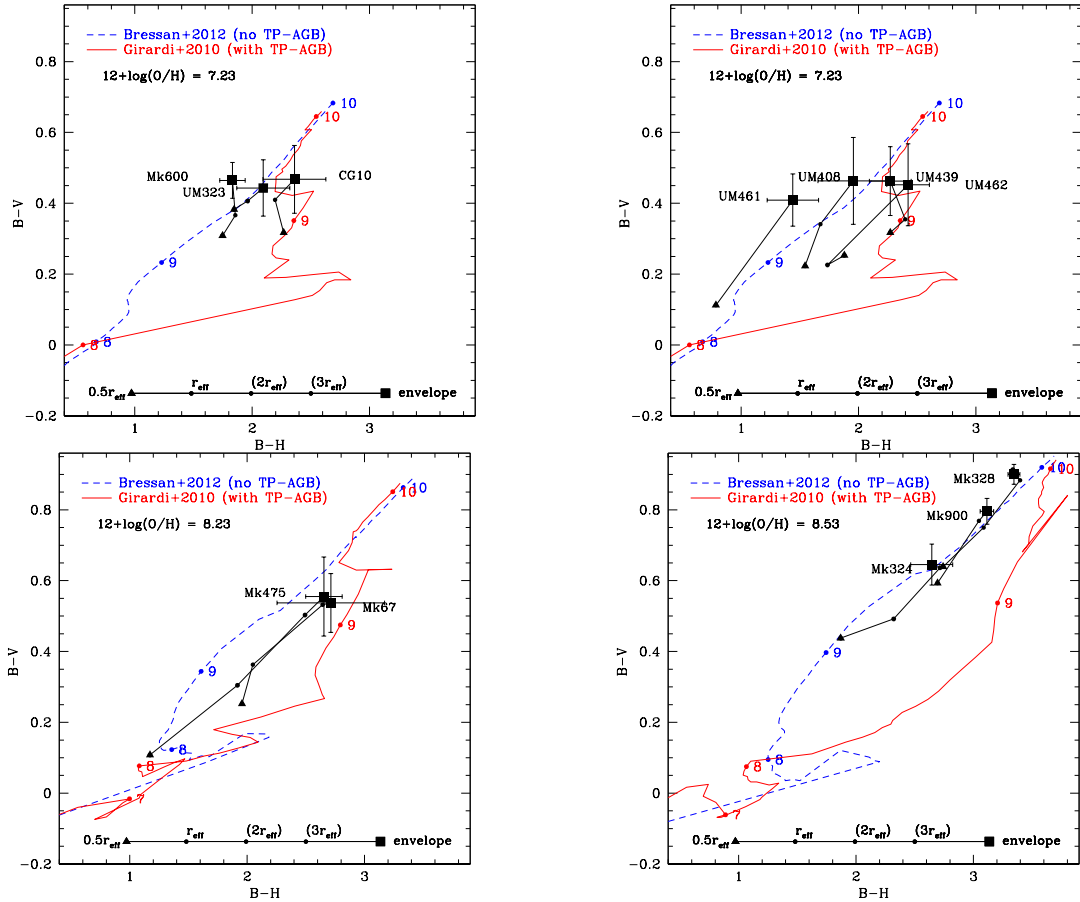


FIG. 6.— Color-color diagrams showing  $B - V$  and  $B - H$  colors at different radii for the BCDs. Black lines connect the color profiles of the BCDs between half of their effective radius (black triangles), through one, two, or three effective radii (small black circles), out to the region used to fit the underlying host galaxies of the BCDs (solid squares). Also shown are SSP single burst models (blue and red lines) and the numbers show the logarithm of the age (in years) of the population at that point. Different panels show different metallicity BCDs and models.

ply the correction factor of 0.7 mag to account for the central flattening of the underlying, older population of stars. We find that the average corrected burst strength of our sample of BCDs is  $\sim 0.8$  mag, with a range of corrected burst strengths from 0.2 mag to 1.5 mag across the sample. This means that the star formation in our BCDs is responsible for average luminosity enhancements of  $\sim 0.8$  mag or about a factor of 2 in luminosity.

Papaderos et al. (1996) also determined the burst strength of their BCDs, and found results similar to ours. Their profile decomposition scheme was substantially more complicated, involving three-component fits to the surface brightness profiles. Even with this difference in methodology, they found that the components associated with the starburst contributed an average of  $\sim 0.75$  mag on top of the underlying host galaxy. Our determination of burst strength is less dependent on assumptions about the profiles of BCDs, since we compare host light to the total observed luminosity of the galaxy, rather than inter-comparing components of the same profile.

In the context of our earlier plots of structural parameters, we stress that this burst strength is too small to account for the displacement of the BCD hosts from the dIs. While the BCD hosts are offset from the dIs in terms of their exponential scale length when measured in the luminosity direction (Figure 3), this offset is  $\sim 2$  mag.

Even if the  $M_B$  values of the BCDs were corrected to remove the light from the starburst and represent only the light from the underlying host galaxy, the BCD hosts would still be distinct from the dIs. Similarly, in terms of central surface brightness, no shift in the luminosity of the BCD hosts can bring them into agreement with the dIs.

## 5. DISCUSSION

In order to understand the evolutionary processes that affect dwarf galaxies, we have carefully measured the structural parameters of the underlying host galaxies in our sample of BCDs and compared them with the structural parameters of a large number of dIs. We emphasize that the structural parameters we have measured are, to the best of our abilities, independent of the existence of the current starburst. The structures of the BCD host galaxies occupy an extreme part of parameter space defined by the structures of dIs. This parameter space covers one and a half orders of magnitude in scale length, and  $\sim 7$  magnitudes (more than a factor of 600) in central surface brightness. This broad parameter space is bounded at one extreme by low surface brightness dwarf galaxies (exceptionally faint  $\mu_{0,B}$  and large  $\alpha_B$  for their luminosities), and at the other extreme by BCD hosts (exceptionally bright  $\mu_{0,B}$  and small  $\alpha_B$  for their luminosities). The BCD hosts are similarly distinctive in the

near-infrared structural parameter diagrams.

The distinctive compactness of the underlying BCD hosts is similar to the results of van Zee et al. (2001) who found that the neutral hydrogen gas (HI) in BCDs is also more centrally concentrated than other gas-rich dwarf galaxies. Van Zee et al. (2001) also found that the rotation curves in BCDs were steeper than in comparable dwarf galaxies, indicating a more compact mass distribution, as well. More recently, Lelli et al. (2014) studied the HI in a sample of dwarf galaxies and found that BCDs have stronger velocity gradients in their inner regions than non-starbursting dwarf galaxies. Lelli et al. (2014) and van Zee et al. (2001) both discuss the persistent nature of this compact structure, even after the current burst of star formation has faded. The unusually compact nature of the stars and gas in these galaxies likely points to a difference in the underlying dark matter distribution of BCDs. Certainly the compact distribution of luminous matter seems to be a hallmark of BCDs; the dark matter distributions are likely to be similarly compact. It may be that this compact matter distribution is the reason BCDs can host such intense starbursts. While BCDs were first identified for their intense star formation activity, the strong starbursts may merely be symptoms of a compact matter distribution. In this way, the compact mass distribution is the fundamental parameter of BCDs, not their intense but transient star formation events.

This structural distinction of the BCD hosts is important both in terms of identifying a well-defined and meaningful sample of present-day BCDs, and also in understanding the past and future evolution of present-day BCDs. There are many possible definitions of BCDs that use various observational criteria ranging from spectral diagnostics to isophotal colors (Sargent & Searle 1970, Thuan & Martin 1981, Gil de Paz & Madore 2005). We suggest that the truly distinctive observable characteristic of BCDs compared with dIs is their exceptionally concentrated underlying mass distribution, as measured by the compact light distribution. This is not a new definition or suggestion, as compactness was part of the original discovery and classification of BCDs by Sargent & Searle (1970). Thuan & Martin (1981) loosely parametrized this compactness by requiring BCDs to have optical sizes  $\sim 1$  kpc. Shortly thereafter, this classification got even broader with the Atlas of Virgo Cluster Dwarf Galaxies (Sandage & Binggeli 1984), where starbursting dwarf galaxies with “several knots and some low surface brightness fuzz” were cataloged as BCDs although the authors acknowledged that “our BCD objects would not fall into the extremes of this class”. The BCD classification continued to grow increasingly broad with time. Loose & Thuan (1986) describe BCDs as “low-luminosity galaxies ... undergoing intense bursts of star formation”, as do more recent groups like Lelli et al. (2012) “...low-mass galaxies that are experiencing a starburst”. The frequently-cited definition in Gil de Paz et al. (2003) parametrizes compactness via the peak surface brightness, and requires  $\mu_{B,\text{peak}} < 22$  mag/arcsec<sup>2</sup>, rather than actually measuring the compactness of the underlying light. Gil de Paz et al. (2003), like many authors, determine these criteria based on their sample of “known” BCDs. Many other authors follow this def-

inition and substitute small size for compactness, and some even classify BCDs purely spectroscopically. As the definition of a BCD has evolved, the importance of compactness has been increasingly overlooked. Our conclusions from this study suggest that the compactness of the underlying light is a defining characteristic of BCDs, and is just as important to their classification as their blue color and their low luminosity.

Even after the current starburst fades (if  $M_B$  fades by perhaps as much as 1 magnitude), the BCD hosts will continue to occupy this extreme area of parameter space. Fading of  $M_B$  can bring BCD hosts closer to the distribution of normal dIs in terms of scale length, but a change in  $M_B$  does not bring the BCD hosts closer to the dIs in terms of central surface brightness. *Major structural changes would be required in the underlying light distribution if BCDs could transform to or from dIs.* This type of transformation would require mechanisms that could cause galaxy-wide structural changes in dwarf galaxies, in particular, changes to the structure of the underlying mass distribution. Among the most frequent mechanisms discussed for transforming the underlying structure of non-interacting dwarf galaxies are substantial mass loss from galactic winds (Mac Low & Ferrara 1999) and infall of fresh gas. In denser environments, interactions with other galaxies can also have transformative effects (e.g., ram pressure and tidal stripping of dwarf spheroids in cluster environments). Ongoing secular structural evolution within the BCDs is not expected to change the underlying structure dramatically enough, as the time scales for internal evolution processes are longer than the other mechanisms discussed. Furthermore, the energy required to remove enough material from the central regions to cause global structural changes is prohibitively large.

Whether this underlying structural distinction is significant enough to truly distinguish BCDs from dIs is a more complicated question which requires additional detailed studies across all types of dwarf galaxies. The broad continuum of structural properties of dwarf galaxies (as seen in the broad parameter space populated by galaxies in both panels of Figure 3) further complicates the classification process, and muddles the evolutionary pathways. One class of dwarf galaxy which may be relevant to these evolutionary connections is the “Transition” type dwarf galaxy (TTD). TTDs have been studied by many groups (Dellenbusch et al. 2008, Koleva et al. 2013, and references therein), and share properties with both the gas-rich classes of dwarf galaxies (dI and BCD) and the gas-poor classes (dE and dSph). It has been suggested that TTDs may possibly represent a short-lived transition period between classes. In some cases, TTDs may be classified as BCDs (e.g., a galaxy with dE-like outer regions but a starburst at its center) or vice versa. While star formation events can alter the appearance of dwarf galaxies, our results suggest that transitions between “true” BCDs and typical dIs would require a significant amount of structural change to the underlying hosts. We consider such transitions unlikely.

Given the apparent permanence of the underlying compact global structure of BCD hosts, and the short gas depletion time scales of the current star formation in BCDs, there must be galaxies which have had a BCD-like phase in their past but which are not forming stars as actively

today. Indeed the galaxies we have identified in Table 3 with similar structural parameters to the BCD hosts may be examples of galaxies which, if starbursting, would be classified as BCDs. Other groups have searched for BCDs before or after their burst phase. Sánchez Almeida et al. (2009) has identified a population of dwarf galaxies in SDSS which may be BCDs during quiescence (QBCDs). QBCDs have some properties in common with BCDs (i.e., similar structure and color of the outskirts) but are not necessarily undergoing a significant burst of star formation. While the sample of 21,000 QBCDs used by Sánchez Almeida et al. may include some examples of BCD-like galaxies in quiescence, they note that the gas-phase abundances of the QBCDs are  $\sim 0.35$  dex more metal rich than BCDs on average, which makes them an unlikely population to transform simply into BCDs with the addition of a starburst. However, the less likely scenario of pristine gas infall might be able to lower their metallicities and trigger a starburst to bring them out of quiescence.

Next we consider the impact of the duty cycle of star formation in BCDs, as today’s BCDs cannot sustain their starbursts indefinitely. Lee et al. (2009) used a volume-limited survey of 261 nearby galaxies (within 11 Mpc) to determine that only  $\sim 6\%$  of dwarf galaxies are currently experiencing global star formation events. In fact, two of our BCDs are nearby enough to be inside the Lee et al. (2009) volume (Mk 36 & Mk 475), and are among the three largest H $\alpha$  equivalent width systems in their entire sample. Even if BCDs have a significantly greater duty cycle of star formation than normal dwarf galaxies, there should be many more non-bursting BCDs than bursting BCDs at any given time. Depending on what triggers the bursts in the BCDs, the pre-burst and post-burst BCDs may have observable signatures, as well. For example, a post-burst BCD would have a unique stellar population for a while as its starburst population becomes intermediate aged. These starburst events themselves may also last longer than is commonly assumed. McQuinn et al. 2010 studied twenty dwarf galaxies and found that most of the starburst durations were between 450-650 Myrs, considerably longer than the lifetimes of O and B stars. Still, we expect the underlying host galaxy structure to change on a slower time scale than that of the starburst, so we could look for galaxies with similarly compact underlying old stellar populations but without current significant star formation (e.g., the types of galaxies listed in Table 3). In principle, surveying for non-bursting dwarf galaxies with compact structural parameters would allow for the determination of the BCD duty cycle. However, carrying out such a study in practice would be very difficult, as it would require detailed observations of a large volume-limited sample.

In addition to classifications of dwarf galaxies based on the structural parameters of their underlying host galaxies, we briefly consider what can be inferred about their evolutionary status by studying their stellar populations. The detailed SED-modeling of the stellar populations and star formation histories of this sample of BCDs will be explored in a subsequent paper, but for now we consider the color gradients found in the BCDs and shown in Figure 6. We find agreement with other groups that the outer regions of BCDs indeed show colors consistent with evolved stellar populations, but it is

revealing to also see how the stellar population changes radially across the galaxy. Marlowe et al. 1999 produced similar plots (their Fig. 7) which showed that the cores of “Blue Amorphous Galaxies” typically have colors consistent with ages of  $\sim 10^8$  years while the outer regions of their underlying host galaxies have colors consistent with ages of  $\sim 10^{10}$  years. Comparing an individual galaxy’s age range (or, analogously, color gradient) from its center to its outskirts may give insight not only about its particular star formation history (SFH) but also about its preferred modes of star formation. These details will be discussed in the context of detailed SFH and stellar mass estimates from our subsequent SED analysis (Janowiecki et al. in preparation).

## 6. ACKNOWLEDGMENTS

We are grateful to S. Salim, L. van Zee, and H. Evans for useful feedback on this work. S.J. also thanks J. Hargis for many useful conversations during the course of this work.

Funding for SDSS-III has been provided by the Alfred P. Sloan Foundation, the Participating Institutions, the National Science Foundation, and the U.S. Department of Energy Office of Science. The SDSS-III web site is <http://www.sdss3.org/>.

SDSS-III is managed by the Astrophysical Research Consortium for the Participating Institutions of the SDSS-III Collaboration including the University of Arizona, the Brazilian Participation Group, Brookhaven National Laboratory, University of Cambridge, Carnegie Mellon University, University of Florida, the French Participation Group, the German Participation Group, Harvard University, the Instituto de Astrofísica de Canarias, the Michigan State/Notre Dame/JINA Participation Group, Johns Hopkins University, Lawrence Berkeley National Laboratory, Max Planck Institute for Astrophysics, Max Planck Institute for Extraterrestrial Physics, New Mexico State University, New York University, Ohio State University, Pennsylvania State University, University of Portsmouth, Princeton University, the Spanish Participation Group, University of Tokyo, University of Utah, Vanderbilt University, University of Virginia, University of Washington, and Yale University.

This research has made extensive use of NASA’s Astrophysics Data System Bibliographic Services. This research has also made use of the NASA/IPAC Extragalactic Database (NED), which is operated by the Jet Propulsion Laboratory, California Institute of Technology, under contract with the National Aeronautics and Space Administration.

This publication makes use of data products from the Wide-field Infrared Survey Explorer, which is a joint project of the University of California, Los Angeles, and the Jet Propulsion Laboratory/California Institute of Technology, and NEOWISE, which is a project of the Jet Propulsion Laboratory/California Institute of Technology. WISE and NEOWISE are funded by the National Aeronautics and Space Administration.

*Facility:* WIYN

## 7. APPENDIX A: WHIRC REDUCTION

Observing extended sources against the high sky background in ground based near-infrared imaging is a great challenge. Near-infrared point source ob-

servations are somewhat more straightforward, but surface photometry requires particular efforts. However, since our target galaxies ( $\sim 1'$ ) are smaller than the full WHIRC field of view ( $\sim 3'$ ), we can still employ relatively simply observing techniques with plenty of well-sampled sky around our targets. This appendix fully describes our reduction process, which is generalizable to any ground-based near-infrared observations of extended sources smaller than the detector field of view. It also describes the process of removing some particular artifacts and features of WHIRC. Much of the process comes from Dick Joyce’s invaluable manual ([www.noao.edu/kpno/manuals/whirc/](http://www.noao.edu/kpno/manuals/whirc/)) and the reduction guide to NEWFIRM ([www.noao.edu/staff/med/newfirm/](http://www.noao.edu/staff/med/newfirm/)), and from a very useful conversation with Janice Lee.

The WHIRC team provides a script (WPREP) that carries out necessary steps on every image from an observing run. In our case, it first applies a linearity correction, since WHIRC and most NIR detectors experience modest gain changes as the pixel wells fill up ( $\sim 4\%$  drop at half well capacity). Next, it applies a rough World Coordinate System (WCS) and trims unnecessary reference columns from one side of the images.

Standard flat field images are not useful on NIR imagers because of the high background from the instrument. Instead, it was recommended to take images of the flat field screen with the flat field lamps both on and off. We took 10 lamps-on and 10 lamps-off in each filter. By subtracting the (average-combined) lamps-off flat from the lamps-on flat in each filter, a true sensitivity correction is obtained. However, we found that our dark sky flats (discussed later) were a much better sensitivity correction to our observations. We did, however, use the lamps-on and lamps-off dome flats to create a bad pixel mask (BPM) with the CCDMASK. Sets of dark exposures were also taken at each exposure time of our science frames, and are median-combined. These darks are necessary to create the dark sky flats.

One of the major customizations to our reduction process facilitates the removal of an intermittent dark “palm-print” feature on the first image of most dither sequences. Our observing program used 4-point dither patterns, and in many cases the first pointing had the dark “palm-print” feature imposed on it. This feature was later determined to be related to the temperature change of the detector when it transitions from idle mode (and is continuously reading out) to exposing mode (no longer reading out, but integrating), and is a short-term transient feature that appeared only in the first dither points. Our iterative sky subtraction is able to successfully model and remove it from the affected images.

As a result of this complication, our sky subtraction method is a three step iterative process, involving three separate sky subtractions. The first sky subtraction is the crudest, involving a single median combination (using only the central 1000x1000 pixels) and subtraction for each set of observations in a particular filter of a particular target. We also generated crude dark sky flats by median-combining all of the science observations from a particular exposure time and filter in a given night, subtracting the appropriate dark frame, and used those rough dark sky flats to flatten the images. This first sky-subtraction is used to identify which images are affected

by the dark “palm-print” feature, and get a rough look at the data, as a raw un-sky-subtracted image is very difficult to interpret.

Once the images affected by the “palm-print” are identified, we begin the second-pass sky subtraction. We use the same method of median combining and subtracting a single sky image for each filter and target, and a simple dark sky flattening for each filter, but this time the images affected by the “palm-print” are left out of the median combinations. We do still subtract the median-sky images from the affected images, though, and are able to assess the consistency and stability of the dark feature, as well as the stability of the sky throughout each dither sequence.

Next we want to combine all of these sky subtracted images for each target. We tried using NEWFIRM’s NFWCS task at this point to refine and improve the WCS on the images, but WHIRC’s small field of view and the scarcity of 2MASS stars in the frame made it fail on most images. Instead, we used the USNO-B2 catalog (Monet et al. 2003) to check and improve the WCS on all of the images. Once the WCS was suitable, we used MSCIMAGE to re-project all of the images for a particular target and filter onto the same pixel scale so that they were aligned. We applied this same re-projection to the original BPMs as well, and used them on the final images. These reprojected sky-subtracted images are then median-combined (using the sky level from the central region as the zero-level in IMCOMBINE) to create our first stacked images of each target.

The added depth of these images allows us to detect and mask objects too faint to be seen in individual frames, to further improve the sky subtraction. We used the ACESEGMENT task to automatically detect and generate a mask for all of the objects in the combined image. These masks are then reprojected using MSCIMAGE back to each of the original images from that dither sequence. Using these detailed masks we generated improved dark sky flats for each filter.

Finally, we begin the final-pass sky subtraction using these detailed masks on every raw image. This final sky subtraction is more sophisticated than the previous sky subtractions since we create a custom sky image for each individual science image. In most cases we created the sky image from a masked weighted median combination of the (usually) 7 nearest (most contemporaneous?) images of the same dither sequence. A combination of the detailed object masks and the bad pixel mask were used on each of the raw images, and the images with the “palm-print” are excluded from the sky image creation. We used the second-pass sky subtraction to assess sky stability and determine whether 5, 7, or 9 images should be used in the median combine. We also weighted each image in the median combination by  $1/\sqrt{n+1}$  where  $n$  is the number of images separating the target image from the sky image in the dither sequence. This weighting method increases the contribution from nearby images and decreases the contribution from more distant images. After subtracting the sky image from each science frame, we flatten the images with the improved dark sky flats created using the detailed masks.

Now we must remove the dark “palm-print” feature from the affected first-images. The sky subtraction on

TABLE 4  
PHOTOMETRIC CALIBRATIONS IN JHK

Term	value	error	Description
$J$	-	-	calibrated $J$ magnitude
$H$	-	-	calibrated $H$ magnitude
$K$	-	-	calibrated $K$ magnitude
$m_J$	-	-	observed instrumental magnitude in $J$ filter
$m_H$	-	-	observed instrumental magnitude in $H$ filter
$m_K$	-	-	observed instrumental magnitude in $K$ filter
$X$	-	-	airmass of observation
$k_J$	0.061	-	standard KPNO airmass extinction coefficient in $J$
$k_H$	0.031	-	standard KPNO airmass extinction coefficient in $H$
$k_K$	0.024	-	standard KPNO airmass extinction coefficient in $K$
$\xi_J$	23.124	0.032	best-fit photometric zero-point in $J$
$\xi_{JH}$	-0.036	0.036	best-fit photometric zero-point in $J - H$
$\xi_{JK}$	0.586	0.032	best-fit photometric zero-point in $J - K$
$\epsilon_J$	0.0238	0.0672	best-fit photometric color term in $J$ equation
$\mu_{JH}$	0.9590	0.0658	best-fit photometric color term in $J - H$ equation
$\mu_{JK}$	1.0653	0.0552	best-fit photometric color term in $J - K$ equation

these images is satisfactory, since only the adjacent non-affected images were used to create the sky images. We median combine all sky-subtracted images in a particular filter that contain the dark feature in order to make a template model of the feature. This template is scaled to precisely match each affected image, by matching median levels in selected regions both on and off the feature. After the template has been scaled to the individual image, the template is subtracted from the image, and the dark “palm-print” feature is removed.

Before the final stacking of dither sequences, we also checked the photometric stability throughout the night by measuring the brightnesses of 2MASS stars in each individual frame. We used this photometry to check for absolute zeropoint variations throughout the night and also be sure that the photometry was stable throughout individual dither sequences. If standard stars are being observed to calibrate the observations, this photometric verification is useful. When we did experience non-photometric conditions, the 2MASS stars in the final stacked image were used to determine a post-calibration zeropoint.

Just before doing the final image stacking, we checked that all of the images have excellent WCS and re-projected them to be mutually aligned. Additionally, we calculate the original sky level of each image (before any sky subtraction was applied) and store it as a header keyword in order to later restore the Poisson image statistics. We use IMCOMBINE to average and ccdclip the images, using both the median of the central 1000x1000 pixels as the zeropoint (which was usually very close to zero) and the offsets from the WCS. After this image is combined, we add a constant value to it in order to make the final sky level the same as the average throughout the sequence.

At this point, the images have been fully reduced and are ready to be measured. The combination of the iterative sky subtraction and object masking (and the dark “palm-print” feature removal) makes these reduced images suitable for surface photometry. An extensive detailed description of the parameters used for each task is available upon request, but it was too detailed to present in this appendix.

In addition to the per-image calibrations from 2MASS, we calibrated many of our observations using JHK standard stars from Hunt et al. (1998). Presented in the table below is a sample of our derived zero-points and color terms, and the values we used for airmass extinction. These values come from observations of 7 standard stars in JHK filters on the night of November 5th 2008. The full set of photometric equations for calibrated  $J$  magnitudes, and  $J - H$  and  $J - K$  colors are given below. Descriptions and values of the adopted and best-fit terms are given in Table 4.

$$J = m_J - Xk_J + \epsilon_J(m_J - m_H) + \xi_J$$

$$J - H = (m_J - Xk_J) - (m_H - Xk_H) + \mu_{JH}(m_J - m_H) + \xi_{JH}$$

$$J - K = (m_J - Xk_J) - (m_K - Xk_K) + \mu_{JK}(m_J - m_K) + \xi_{JK}$$

Sample images and detailed descriptions of observing and reducing WHIRC data are given on the website ([www.noao.edu/kpno/manuals/whirc/WHIRC.html](http://www.noao.edu/kpno/manuals/whirc/WHIRC.html)) and were invaluable in our data reduction process.

#### REFERENCES

- Ahn, C. P., Alexandroff, R., Allende Prieto, C., et al. 2012, ApJS, 203, 21  
 Alam, M. S., & Predina, J. P. 1999, Proc. SPIE, 3701, 296  
 Aloisi, A., Clementini, G., Tosi, M., et al. 2007, ApJ, 667, L151  
 Amorín, R., Aguerrí, J. A. L., Muñoz-Tuñón, C., & Cairós, L. M. 2009, A&A, 501, 75  
 Amorín, R. O., Muñoz-Tuñón, C., Aguerrí, J. A. L., Cairós, L. M., & Caon, N. 2007, A&A, 467, 541  
 Binggeli, B., & Cameron, L. M. 1991, A&A, 252, 27  
 Binggeli, B., Sandage, A., & Tarenghi, M. 1984, AJ, 89, 64  
 Bressan, A., Marigo, P., Girardi, L., et al. 2012, MNRAS, 427, 127  
 Brinchmann, J., Pettini, M., & Charlot, S. 2008, MNRAS, 385, 769  
 Cardamone, C., Schawinski, K., Sarzi, M., et al. 2009, MNRAS, 399, 1191

- Carter, D., Smith, D. J. B., Percival, S. M., et al. 2009, *MNRAS*, 397, 695
- Dellenbusch, K. E., Gallagher, J. S., III, Knezek, P. M., & Noble, A. G. 2008, *AJ*, 135, 326
- Doublier, V., Caulet, A., & Comte, G. 1999, *A&AS*, 138, 213
- Garland, C. A., Pisano, D. J., Williams, J. P., Guzmán, R., & Castander, F. J. 2004, *ApJ*, 615, 689
- Gil de Paz, A., & Madore, B. F. 2005, *ApJS*, 156, 345
- Gil de Paz, A., Madore, B. F., & Pevunova, O. 2003, *ApJS*, 147, 29
- Graham, A. W. 2013, *Planets, Stars and Stellar Systems. Volume 6: Extragalactic Astronomy and Cosmology*, 91
- Herrmann, K. A., Hunter, D. A., & Elmegreen, B. G. 2013, *AJ*, 146, 104
- Hunt, L. K., Mannucci, F., Testi, L., et al. 1998, *AJ*, 115, 2594
- Hunter, D. A., & Elmegreen, B. G. 2006, *ApJS*, 162, 49
- Izotov, Y. I., & Thuan, T. X. 2004, *ApJ*, 616, 768
- Izotov, Y. I., Thuan, T. X., & Stasińska, G. 2007, *ApJ*, 662, 15
- Jedrzejewski, R. I. 1987, *MNRAS*, 226, 747
- Jester, S., Schneider, D. P., Richards, G. T., et al. 2005, *AJ*, 130, 873
- Koleva, M., Bouchard, A., Prugniel, P., De Rijcke, S., & Vauglin, I. 2013, *MNRAS*, 428, 2949
- Kormendy, J. 1977, *ApJ*, 218, 333
- Lagos, P., Telles, E., Nigoche-Netro, A., & Carrasco, E. R. 2011, *AJ*, 142, 162
- Lee, J. C., Kennicutt, R. C., Jr., Funes, S. J. J. G., Sakai, S., & Akiyama, S. 2009, *ApJ*, 692, 1305
- Lelli, F., Fraternali, F., & Verheijen, M. 2014, *A&A*, 563, A27
- Lin, D. N. C., & Faber, S. M. 1983, *ApJ*, 266, L21
- Lisker, T. 2009, *Astronomische Nachrichten*, 330, 1043
- Loose, H.-H., & Thuan, T. X. 1986, *ApJ*, 309, 59
- Mac Low, M.-M., & Ferrara, A. 1999, *ApJ*, 513, 142
- Marlowe, A. T., Meurer, G. R., & Heckman, T. M. 1999, *ApJ*, 522, 183
- McCall, M. L., Vaduvescu, O., Pozo Nunez, F., et al. 2012, *A&A*, 540, A49
- McGaugh, S., & Schombert, J. 2013, *arXiv:1303.0320*
- McQuinn, K. B. W., Skillman, E. D., Cannon, J. M., et al. 2010, *ApJ*, 724, 49
- Meixner, M., Smee, S., Doering, R. L., et al. 2010, *PASP*, 122, 451
- Micheva, G., Östlin, G., Bergvall, N., et al. 2013, *MNRAS*, 431, 102
- Monet, D. G., Levine, S. E., Canzian, B., et al. 2003, *AJ*, 125, 984
- Mould, J. R., Huchra, J. P., Freedman, W. L., et al. 2000, *ApJ*, 529, 786
- Noeske, K. G., Papaderos, P., Cairós, L. M., & Fricke, K. J. 2005, *A&A*, 429, 115
- Noeske, K. G., Papaderos, P., Cairós, L. M., & Fricke, K. J. 2003, *A&A*, 410, 481
- Papaderos, P., Guseva, N. G., Izotov, Y. I., & Fricke, K. J. 2008, *A&A*, 491, 113
- Papaderos, P., Loose, H.-H., Fricke, K. J., & Thuan, T. X. 1996, *A&A*, 314, 59
- Parodi, B. R., Barazza, F. D., & Binggeli, B. 2002, *A&A*, 388, 29
- Patterson, R. J., & Thuan, T. X. 1996, *ApJS*, 107, 103
- Pildis, R. A., Schombert, J. M., & Eder, A. 1997, *ApJ*, 481, 157
- Pustilnik, S. A., Martin, J.-M., Tepliakova, A. L., & Kniazev, A. Y. 2011, *MNRAS*, 417, 1335
- Sánchez Almeida, J., Aguerri, J. A. L., Muñoz-Tuñón, C., & Vazdekis, A. 2009, *ApJ*, 698, 1497
- Salzer, J. J., & Norton, S. A. 1999, *The Low Surface Brightness Universe*, 170, 253
- Salzer, J. J., Williams, A. L., & Gronwall, C. 2009, *ApJ*, 695, L67
- Sandage, A., & Binggeli, B. 1984, *AJ*, 89, 919
- Sargent, W. L. W., & Searle, L. 1970, *ApJ*, 162, L155
- Schlafly, E. F., & Finkbeiner, D. P. 2011, *ApJ*, 737, 103
- Searle, L., Sargent, W. L. W., & Bagnuolo, W. G. 1973, *ApJ*, 179, 427
- Searle, L., & Sargent, W. L. W. 1972, *ApJ*, 173, 25
- Sharina, M. E., & Il'ina, E. A. 2013, *Astronomische Nachrichten*, 334, 773
- Staveley-Smith, L., Davies, R. D., & Kinman, T. D. 1992, *MNRAS*, 258, 334
- Thuan, T. X. 1985, *ApJ*, 299, 881
- Thuan, T. X., & Martin, G. E. 1981, *ApJ*, 247, 823
- Thuan, T. X., Izotov, Y. I., & Foltz, C. B. 1999, *ApJ*, 525, 105
- van Dokkum, P. G. 2001, *PASP*, 113, 1420
- van Zee, L. 2001, *AJ*, 121, 2003
- van Zee, L., Salzer, J. J., & Skillman, E. D. 2001, *AJ*, 122, 121
- Werk, J. K., Jangren, A., & Salzer, J. J. 2004, *ApJ*, 617, 1004
- Wright, E. L., Eisenhardt, P. R. M., Mainzer, A. K., et al. 2010, *AJ*, 140, 1868
- Zhao, Y., Gao, Y., & Gu, Q. 2010, *ApJ*, 710, 663